Geochemistry, Geophysics, Geosystems

RESEARCH ARTICLE
10.1029/2020GC009297

Special Section:
Tethyan dynamics: from rifting to collision

# Tectonic Controls on Block Rotation and Sheeted Sill Emplacement in the Xigaze Ophiolite (Tibet): The Construction Mode of Slow-Spreading and Ultraslow-Spreading Oceanic Crusts

**Tong Liu[1], Henry J. B. Dick[2], Chuan-Zhou Liu[1,3,4,5], Fu-Yuan Wu[1,4], Wen-Bin Ji[6], Chang Zhang[1], Wei-Qi Zhang[1,4], Zhen-Yu Zhang[1,4], Yin-Zheng Lin[1,4], and Zhen Zhang[1,4]**

[1]State Key Laboratory of Lithospheric Evolution, Institute of Geology and Geophysics, Chinese Academy of Sciences, Beijing, China, [2]Department of Geology and Geophysics, Woods Hole Oceanographic Institution, Woods Hole, Massachusetts, USA, [3]CAS Center for Excellence in Tibetan Plateau Earth Sciences, Beijing, China, [4]College of Earth and Planetary Sciences, University of Chinese Academy of Sciences, Beijing, China, [5]Laboratory for Marine Geology, Qingdao National Laboratory for Marine Science and Technology, Qingdao, China, [6]Department of Geology, Northwest University, Xi'an, China

**Abstract** The internal structure of oceanic crusts is not well understood due to the limitation of deep drilling. However, that of ophiolites, i.e., on-land ancient analogs of oceanic lithosphere, could be precisely mapped and measured. The Xigaze ophiolite in Tibet has been regarded as "peculiar", due to the sheeted sill complex in its upper crust, and non-sheeted diabase sills/dikes crosscutting its mantle and lower crust, which are geometrically different from the primarily vertical sheeted dike complex. Based on extensive field observations, here we present petrological and geochemical data for the Xigaze ophiolite to decipher the origin of sheeted sill complex and its implications for the construction of oceanic crusts. Diabases in the Xigaze ophiolite could be subdivided into sheeted sills, Group 1 non-sheeted dikes, and Group 2 non-sheeted sills, based on their orientations. These diabases cut other lithologies, and hence belong to the latest-stage products. Based on petrological, geochemical, and structural data, we highlight the important role of detachment fault in the generation of sheeted and non-sheeted sills. During the formation of oceanic crust, large block exhumation, multi-stage rotations, and foundering are argued here as key mechanisms for the generation of Xigaze sheeted and non-sheeted dikes/sills, all of which are in the evolution of detachment fault systems. These processes are also not uncommon for asymmetrical segments at modern slow-spreading and ultraslow-spreading ridges, but are rare at symmetrical segments. Due to the evolution of detachment fault, the internal structures of (ultra)slow-spreading ridges are more complex than those at fast-spreading ridges.

**Key Points:**

- The Xigaze ophiolite develops the peculiar sheeted sill complex, which is geometrically different from sheeted dike complex
- Generation of sheeted sills is controlled by block exhumation, rotation, and foundering, which are associated with detachment faults
- Construction of slower-spreading oceanic crusts is quite complex, and directly controlled by the evolution of detachment faults

**Supporting Information:**

- Supporting Information S1
- Figure S1

**Correspondence to:**
T. Liu,
liutong@mail.iggcas.ac.cn

**Citation:**
Liu, T., Dick, H. J. B., Liu, C.-Z., Wu, F.-Y., Ji, W.-B., Zhang, C., et al. (2021). Tectonic controls on block rotation and sheeted sill emplacement in the Xigaze ophiolite (Tibet): The construction mode of slow-spreading and ultraslow-spreading oceanic crusts. *Geochemistry, Geophysics, Geosystems*, *22*, e2020GC009297. https://doi.org/10.1029/2020GC009297

Received 14 JUL 2020
Accepted 20 JAN 2021



## 1. Introduction

The construction of oceanic crusts, transferring vast energy and mass from the Earth's interior to the seafloor, is one of the most important geological processes on planet Earth. Oceanic crustal architectures can be directly investigated at modern mid-ocean ridges via deep drilling, and can also be precisely mapped in ophiolites (e.g., Dick et al., 2006; Karson, 2018; Snow & Edmonds, 2007). Ophiolites have been genetically linked to oceanic lithospheres since the recognition of sheeted dike complex, whose formation needs continuous spreading and magma injection (e.g., Gass, 1968; Moores & Vine, 1971). Sheeted dike complexes comprise >90% diabase dikes that originally lie vertically and are perpendicular to the major lithology boundaries of oceanic crusts (Figure 1a) (Karson, 2018). These sheeted diabases represent upper crustal fractures, where magmas move continuously from the lower crust to feed the upper crustal extrusive lavas (Hopson, 2007; Karson, 2018). Thus, formation mechanism of sheeted dike complexes is key to understanding the construction of oceanic crusts. Sheeted dike complexes have been well studied and precisely mapped in several ophiolites, such as the Troodos ophiolite in Cyprus and Semail ophiolite in Oman (e.g., France et al., 2009; MacLeod & Rothery, 1992; Moores & Vine, 1971; Nicolas et al., 2008), of which internal structures match well crustal architectures at the East Pacific Rise (EPR) (e.g., France et al., 2009; Karson, 2018). These observations collectively improved the recognition of vertical sheeted dikes within the horizontally layered oceanic crusts (Figure 1a) (e.g., Karson, 2018; Sinton & Detrick, 1992).

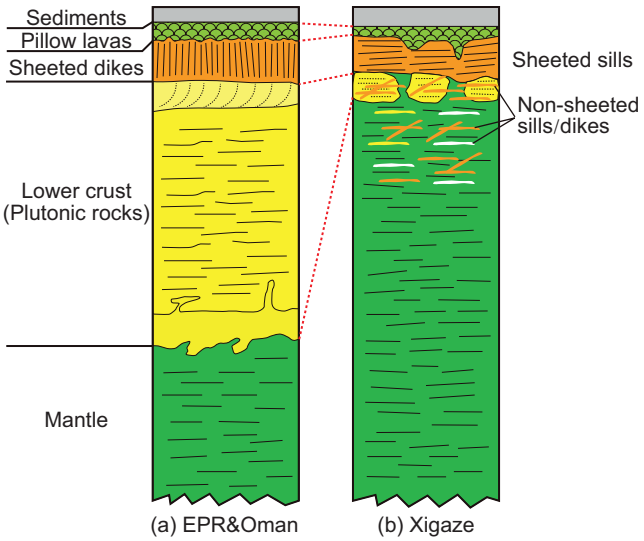


**Figure 1.** Oceanic crustal architectures shown in pseudostratigraphy. (a) The East Pacific Rise (EPR) and Oman ophiolite show a horizontally layered structure with the occurrence of vertical sheeted dikes (after Nicolas et al., 1988). (b) The Xigaze ophiolite has sheeted sills in its upper crust and non-sheeted mafic sills/dikes crosscutting its mantle and lower crust (after Nicolas et al., 1981).

However, the Xigaze ophiolite in the Tibetan Plateau shows a different picture from the Oman and Troodos ophiolites. It develops "peculiar" sheeted sill complex in its upper crust and non-sheeted, discrete diabase sills/dikes crosscutting its mantle and lower crust (Nicolas et al., 1981). The "sheeted sill complex" is defined to describe those sheeted diabases that strike concordantly to the ophiolite pseudostratigraphy, and to the gabbro and mantle foliations (Figure 1b), a geometry fundamentally different from that of sheeted dikes (Hopson, 2007; Nicolas et al., 1981). The sheeted sill complex, along with the non-sheeted sills/dikes, is truly a tectonic enigma in extensional environments, where dikes are modeled to lie perpendicular to the minimum stress along the spreading directions of ocean basins (Anderson, 1951). Hopson (2007) suggested that the sheeted sills in the Xigaze ophiolite were generated in an axial melt lens typical of fast-spreading ridges, hence showing sill-like occurrences. However, such an explanation is incompatible with the geological features of the Xigaze ophiolite, i.e., large-scale mantle but with minor crust, and discontinuous exposures of lower crust, which support its formation at a low rate of magma supply in a slow-spreading ridge setting (Girardeau et al., 1985a; Liu et al., 2018; Nicolas et al., 1981). Therefore, the mechanism generating the sheeted sill complex, and its implication for the construction of oceanic crusts remain unclear.

Based on extensive field observations, we present petrological and geochemical data of the sheeted sill complex and lower crustal gabbros in the Xigaze ophiolite. Our results show that the sheeted sill complex of the Xigaze ophiolite is not as "peculiar" as previously suggested, but could be explained by geological processes in the context of slower-spreading ocean ridges, and thus provides supplementary information on understanding of the geometry and construction of modern slow-spreading and ultraslow-spreading oceanic crusts, which are still poorly studied.

## 2. Geology of the Xigaze Ophiolite

The Xigaze ophiolite crops out in the central part of the Yarlung Zangbo suture zone in southern Tibet, which marks the closure of Neo-Tethys Ocean and the surface boundary between the Indian and Eurasian plates (e.g., Bao et al., 2013; Hébert et al., 2012; Wu et al., 2014; Yin & Harrison, 2000). Well-exposed massifs, including Jiding, Luqu, Deji, Bainang, Baigang, and Dazhuqu, crop out continuously from west to east in the Xigaze ophiolite (Figure 2a). These massifs collectively have a complete ophiolite sequence, composed of mantle peridotites, gabbroic rocks, diabase dikes and sills, and pillow and massive lavas, but show variable crustal thicknesses ranging from ~2 to 3 km to even missing (Nicolas et al., 1981). Mantle peridotites have experienced variable degrees of serpentinization, while fresh harzburgites/lherzolites only locally occur in the Luqu and Dazhuqu massifs (e.g., Liu et al., 2019; Zhang et al., 2017). Gabbroic rocks occur in three massifs, i.e., Jiding, Baigang, and Dazhuqu, which are only hundreds of meters thick (Bao et al., 2013; Girardeau et al., 1985a; Liu et al., 2018). The mantle peridotites and gabbroic rocks both are pervasively cut by discrete diabase dikes and sills, which increase northwards in proportion, and transfer gradationally into total diabase units. These diabases show subparallel orientations with the magmatic foliations of gabbroic rocks, the primary high-temperature foliations of mantle peridotites, and also with the nearly E–W-trending major unit boundaries of the ophiolite (i.e., mantle–gabbro boundary), hence were termed "sheeted sills" (Girardeau et al., 1985a; Hopson, 2007; Nicolas et al., 1981). High-precision geochronological data have shown that the gabbros and diabases of the Xigaze ophiolite formed nearly synchronously, in a short duration of ~124–130 Ma (see the review by Liu et al. (2016)).

The geological features of the Xigaze ophiolite were regarded as "peculiar" with respect to those of the Oman and Troodos ophiolites (Nicolas et al., 1981), and were summarized by previous studies as: (1) large-scale highly serpentinized mantle peridotites with small amounts of crustal rocks, (2) laterally discontinuous

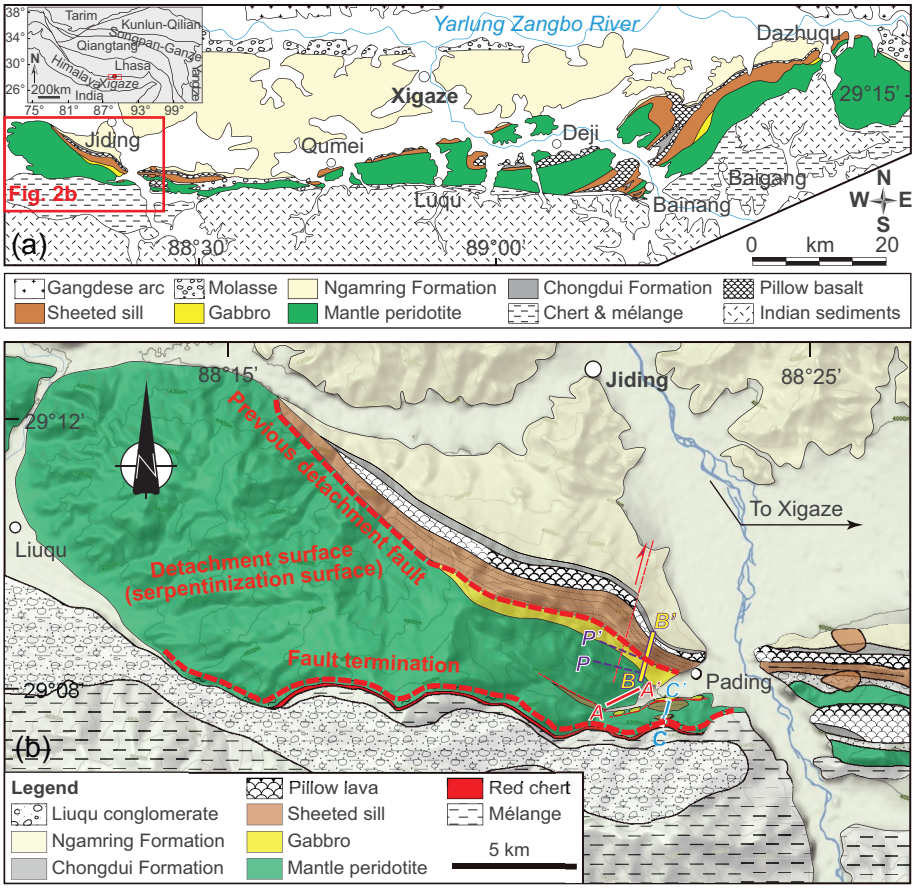


**Figure 2.** Geological maps. (a) Simplified geological map of the Xigaze ophiolite, southern Tibet. (b) Geological map of the Jiding massif in the western part of Xigaze ophiolite, showing in situ geological sections measured in this study (see the text for details). The occurrence and location of oceanic detachment fault are shown here, with details referring to the discussion.

lower crustal units, i.e., gabbroic rocks, (3) the occurrence of sheeted sill complex rather than sheeted dikes, and (4) the pervasive diabases cutting gabbroic and mantle rocks (Bao et al., 2013; Girardeau et al., 1985a; Liu et al., 2016, 2018; Nicolas et al., 1981; Wu et al., 2014). These features were interpreted as formation at a low magma supply, which was probably at an (ultra)slow-spreading ridge (Girardeau et al., 1985a; Liu et al., 2016, 2018; Nicolas et al., 1981). Besides, the recognition of oceanic detachment fault, which is an exclusive feature of (ultra)slow-spreading ridges (Blackman et al., 2009), in the Xigaze ophiolite by paleomagnetic and structural studies also attested to these arguments (Li et al., 2016; Maffione et al., 2015).

## 3. In Situ Observations of the Jiding Massif in the Xigaze Ophiolite

Geological mapping and two-dimensional structural measurements were done in this study at the Jiding massif, which has a complete sequence cropping out in the western part of the Xigaze ophiolite (Figure 2). Detailed geological sections include the A-A′ and B-B′ sections in the northern part, and C-C′ section in the southern part (Figure 2b). The A-A′ section for the mantle unit (its details not shown here) is about 1.2-km long in a NEE60° direction, where mantle peridotites are heavily serpentinized and occasionally intruded by a series of meters-thick dikes and sills of rodingites, foliated gabbros, amphibolites, and diabases (Figure S1). Foliated gabbros have experienced variable extents of amphibolite-facies metamorphism, and contain clinopyroxene relicts, brown amphibole, altered plagioclase, and minor ilmenites (Figure 5a). They display crystal preferred orientations of amphiboles and clinopyroxenes (Figure 5a). Amphibolites have similar mineral assemblages to foliated gabbros, but contain more modal amphiboles with respect to

clinopyroxenes (Figure 5b). The minerals in amphibolites are also intensely sheared and deformed, with recrystallized plagioclases, showing a protomylonitic texture (Figure 5b).

The 1574.5-m thick B-B′ section in a direction of NNE14.5° starts at the serpentinized mantle peridotites (236 m, shown in B-P section in detail), through lower crust (353 m, shown in P-P′ section in detail), sheeted sill complex (774 m), and pillow lavas (211.5 m) to the fault contact with the overlying siliceous mudrocks of the Chongdui Formation, which is in the lower part of the Xigaze fore-arc basin sediments (Figures 3 and 4a). Mantle peridotites in this section are variably altered into serpentinites, and are intruded pervasively by diabase sills and dikes, a few of which are subject to amphibolite-facies metamorphism (Figure 4b). Occasionally, fresh diabase dikes are observed intruding into serpentinized mantle peridotites, where the former show clear two-way chilled margins (Figure 4c). Gabbroic rocks from the P-P′ lower crustal section show clear layering or magmatic foliations, dipping moderately to steeply (58–87°) to the north (NW345–NNE25°). They are predominantly gabbros, with a few olivine gabbros and gabbronorites, generally having fine-grained to medium-grained (~1–2 mm) olivine, clinopyroxene, orthopyroxene, and altered plagioclase crystals (Figures 5c and 5d), but with local course-grained to pegmatitic gabbros. Oxide-bearing gabbros also occur at the top of lower crust, covering ~8% of the total P-P′ section (Figure 3). They contain fine-grained to medium-grained clinopyroxene, altered plagioclase, and minor ilmenites, in which some clinopyroxene crystals experienced low-temperature alteration into amphiboles (Figure 5e). Point counting shows that ilmenite in the oxide-bearing gabbros has a modal content of ~0.25–2%, hence they are defined as disseminated oxide gabbros, based on the classification of Dick et al. (2002). These disseminated oxide gabbros typically show an isotropic texture, without evidence for deformation. All types of gabbroic rocks are intruded pervasively by diabase sills and dikes of variable thicknesses (~0.2–14 m), with a gabbro–diabase proportion of 2:1 (Figure 3). These diabases have orientations mainly subparallel with, but occasionally oblique to the gabbro foliations, dipping consistently with each other (Figures 4d and 4e). Besides, intersected diabase dikes and sills are locally observed intruding gabbros (Figure 4f), suggesting multi-stage melt intrusions into the gabbros. The boundaries between diabases and gabbros are variable, either in an arborization shape or being curved (Figures 4g and 4h). The sheeted sill complex to the north of the P-P′ section is in intrusive contact with gabbros, and is composed of 100% diabase sills dipping moderately to steeply to the north (averagely N6°, $n = 9$), an orientation consistent with those sills cutting gabbroic rocks (Figure 4i). All diabases are subject to moderate-temperature to low-temperature alterations, and are composed of green amphibole, altered plagioclase, ilmenite, and a few clinopyroxene relicts (Figure 5f). Amphiboles occur occasionally as rims or coronas of clinopyroxenes, while ilmenites are mostly as skeleton crystals along amphibole cleavages (Figures 5f and 5g). The sheeted diabases are in fault contact with the pillow basalts to the north, which show similar mineral assemblages and alteration degrees to the diabases, but with an intergranular or porphyritic texture (Figure 5h).

The 687.5-m thick C-C′ section, also in a direction of NNE14.5°, starts at the fault contact between the red chert in the south and serpentinized mantle peridotites in the north (Figure 4j). The whole section includes, from south to north, mantle peridotites (226 m), sheeted sill complex (363.5 m), and deformed pillow and massive lavas (98 m) (Figures 3 and 4j). Gabbroic rocks are lacking between mantle peridotites and sheeted sill complex, but occur to the north of the deformed basaltic lavas, in fault contact with each other. Mantle peridotites are intruded by numerous diabase and a few gabbro sills and dikes, dipping moderately to steeply to the south (averagely S174°, $n = 7$). The sheeted sill complex is composed of nearly 100% diabases, with only ~2-m-thick isotropic gabbros. The diabases and isotropic gabbros have intrusive contacts, some of which show one-way chilled margins (Section D in Figure 3). In general, the diabases have mineral assemblages and alteration degrees that are similar to those in the B-B′ section.

Field structural measurements for the Jiding B-B′ section shows variable orientations of diabases and gabbros (Figure 6). Diabases in the sheeted sill complex have strikingly identical orientations with the average orientations of gabbro foliations. In contrast, those non-sheeted, discrete diabase sills/dikes (both in the mantle and lower crust) could be subdivided into two groups. Group 1, containing only a few samples, shows orientations that are subperpendicular to the magmatic foliations of gabbros; while Group 2 overlaps the gabbros in structural elements (Figure 6). Moreover, the gabbros, sheeted sills, and Group 2 non-sheeted sills all have orientations that are compatible with the primary high-temperature foliations of the Jiding mantle peridotites (striking at E95° in average; measured by Girardeau et al., 1985b). These structural data

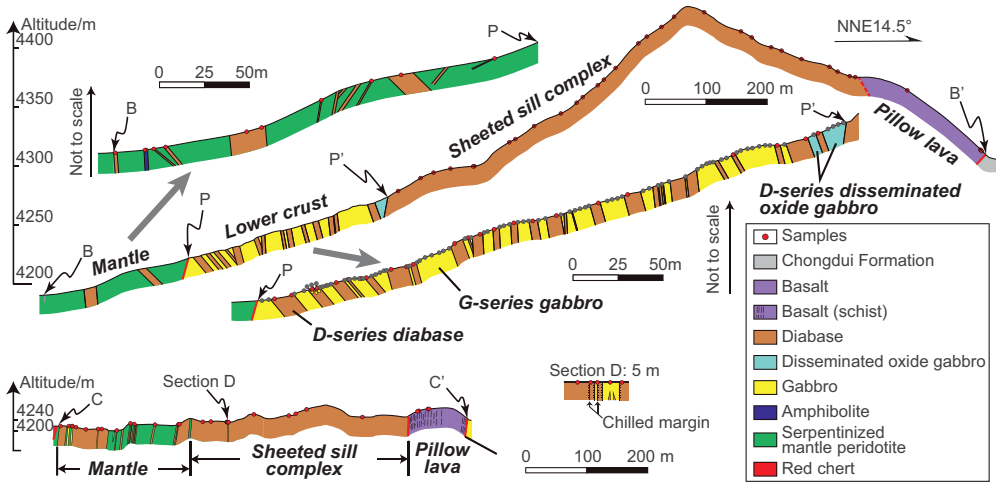


**Figure 3.** Accrete geological sections measured for the Jiding massif. Insets show details of the B-P mantle and P-P′ lower crustal sections. See the text for details of the definition of G-series gabbro, and D-series diabase and disseminated oxide gabbro.

show that the diabases in the Jiding massif occur mainly as sills, occasionally as dikes, among which the former are consistent with the argument of "sheeted sill complex" in previous studies (Girardeau et al., 1985a; Hopson, 2007; Nicolas et al., 1981).

## 4. Analytical Methods

### 4.1. Whole-Rock Major and Trace Element Analyses

Whole-rock major element analysis was conducted at the Institute of Geology and Geophysics, Chinese Academy of Sciences (IGGCAS) in Beijing, China. Before analysis, 0.5 g sample powder was mixed sufficiently with 5 g $Li_2B_4O_7$, and then was fused to make glass discs for analysis on an AXIOS Minerals X-ray fluorescence (XRF) spectrometer. According to triplicate measurements for USGS standard GSR-1, the 95% confidence limits for analysis are $<\pm 0.05\%$ for all oxides, and the total error is less than $\pm 1\%$ (Liu et al., 2019). Another 0.5 g sample powder was heated in an oven at ~1,000°C for 1.5 h, and then was weighted to calculate the relative weight loss for the determination of loss on ignition (LOI).

Whole-rock trace element analysis was done on an Agilent 7500a mass spectrometer in the MC-ICPMS laboratory at the IGGCAS. Before analysis, 50 mg sample powder was dissolved by a mixed acid of distilled $HNO_3$, HF, and $HClO_4$ in Teflon and high-pressure bombs at 195°C for 2 days. The solution was evaporated and dissolved again, using distilled $HNO_3$ to remove HF, and was then heated in 6 N $HNO_3$ at 165°C for 1 day. After total dissolution, the sample was diluted to 100 g by adding 1 g Rh internal standard and additional Milli-Q water. USGS standards BCR-2 and BHVO-2 were measured during the whole procedure, and gave an analytical accuracy better than 5% for most elements.

### 4.2. Mineral Major and Trace Element Analyses

Clinopyroxene, plagioclase, amphibole, and ilmenite major elements were measured on a JEOL JXA8100 instrument at the IGGCAS. Wavelength-dispersive spectrometer (WDS) was used for quantitative measurements. An accelerating voltage of 15 kV and a beam current of 20 nA were used during analysis with the beak and background counting time of 20 s and 10 s, respectively. Oxides of Si, Ti, Al, Cr, Fe, Mn, Mg, Ca, Na, K, and Ni were determined for clinopyroxene, plagioclase, and ilmenite, and additional F and Cl were also measured for amphibole, using natural minerals and synthetic oxides as standards (Liu et al., 2019). An on-line correction for all raw data was processed using a JEOL-modified ZAF procedure (atomic number, absorption, fluorescence).

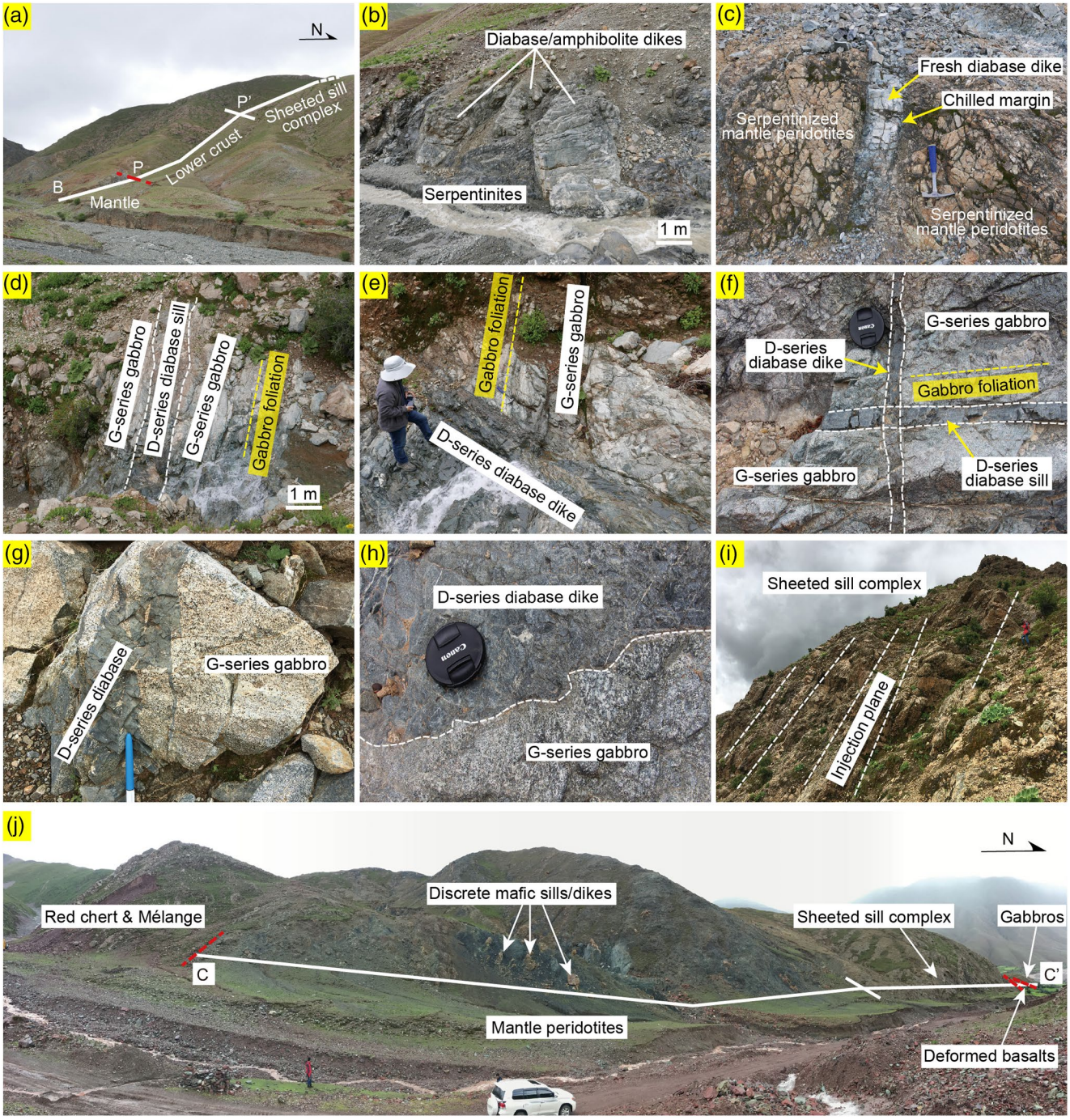


**Figure 4.** Field photos of the B-B′ and C-C′ sections for the Jiding massif. (a) Mantle, lower crust, and sheeted sill complex in the B-B′ section. (b) A series of diabase/amphibolite dikes cut serpentinized mantle peridotites (B-B′). (c) A fresh diabase dike cuts serpentinized mantle peridotites (B-B′). The dike shows clear two-way chilled margins. (d) An ~1 m thick diabase sill intruded into foliated gabbros, showing subparallel orientations with each other (P-P′). (e) A diabase dike cuts obliquely foliated gabbro (P-P′). (f) Intersected diabase dikes and sills are locally found intruding gabbros (P-P′). (g, h) The boundaries between diabases and gabbros are variable, either in an arborization shape or being curved (P-P′). (i) The sheeted sill complex of the Jiding massif comprising 100% diabase sills (B-B′). (j) The C-C′ section starts from the fault contact between red chert and mantle peridotites, through sheeted sill complex, to the fault contact between deformed basalts and gabbros.

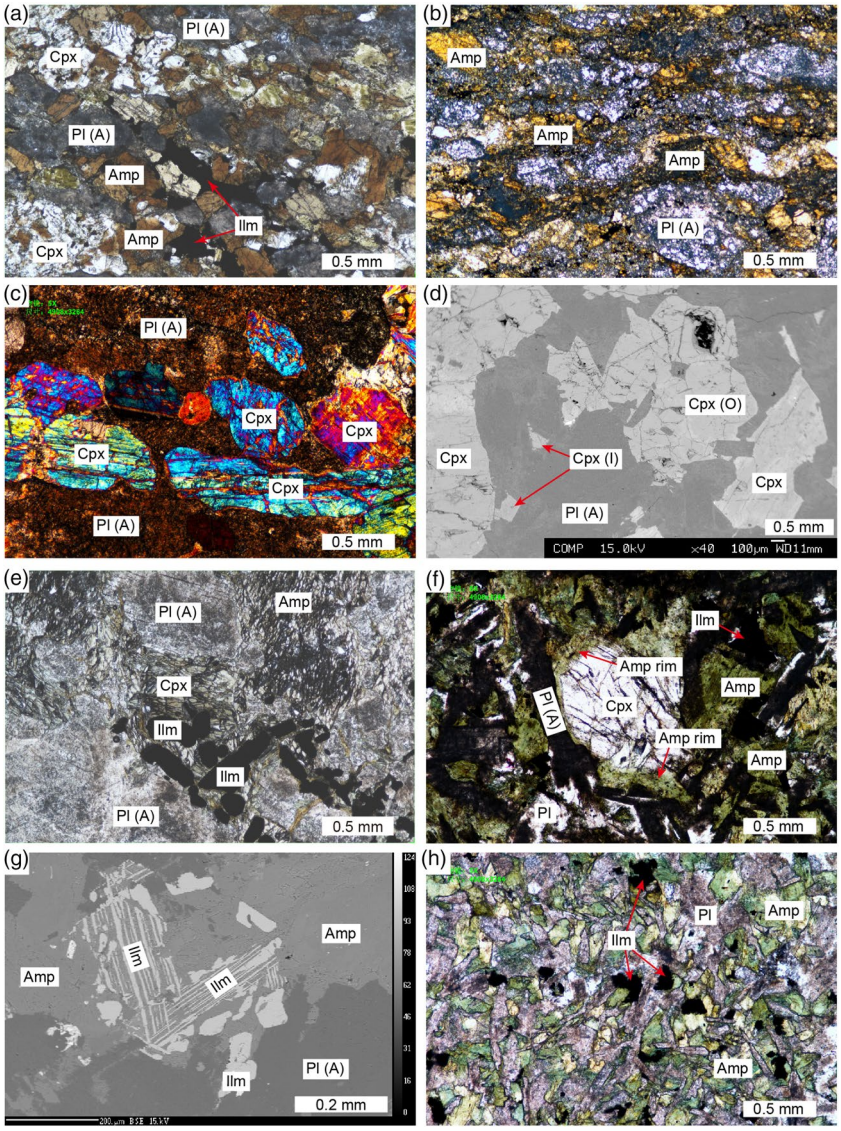


**Figure 5.** Photomicrographs of representative mafic rocks from the Jiding massif. (a) A-A′ section: a foliated gabbro dike in the serpentinized mantle peridotites contains clinopyroxene, brown amphibole, altered plagioclase, and minor ilmenites, showing variable foliations. (b) A-A′ section: amphibolites in the serpentinite matrix contain deformed and recrystallized amphiboles around altered plagioclases. (c) P-P′ section: gabbro shows clear magmatic foliations, with shape preferred oriented clinopyroxenes and totally altered plagioclases. (d) P-P′ section: clinopyroxenes in gabbros occur as oikocrysts including small grains of plagioclases, or interstitial to altered plagioclases (BSE image). (e) P-P′ section: disseminated oxide gabbro contains clinopyroxene, altered plagioclase, and minor ilmenites, showing an isotropic texture. Clinopyroxenes are locally altered and transformed into amphiboles. (f) B-B′ section: diabase comprises clinopyroxene relicts, altered plagioclases, green amphiboles, and ilmenites. Note that some amphiboles occur as rims or coronas of clinopyroxenes. (g) B-B′ section: ilmenites in diabases occur mostly as skeleton crystals along amphibole cleavages (BSE image). (h) B-B′ section: pillow basalts are composed of plagioclases, green amphiboles, and minor ilmenites, showing intergranular textures. Pl: plagioclase, Pl (A): altered plagioclase, Cpx: clinopyroxene, Cpx (O): clinopyroxene oikocrysts, Cpx (I): interstitial clinopyroxene, Amp: amphibole, Ilm: ilmenite.

Clinopyroxene trace element compositions of the Jiding gabbros were analyzed by laser ablation-inductively coupled plasma-mass spectrometry (LA-ICP-MS), employing an Agilent 7500a spectrometry and a 193 nm ArF excimer LA system at the MC-ICPMS Laboratory, IGGCAS. Isotopes were measured using a peak-hopping mode, with a laser diameter of ca. 90–120 μm, and an 8 Hz repetition rate. A NIST 610 glass standard was used for external calibration, and a NIST 612 standard was used for analysis monitoring.

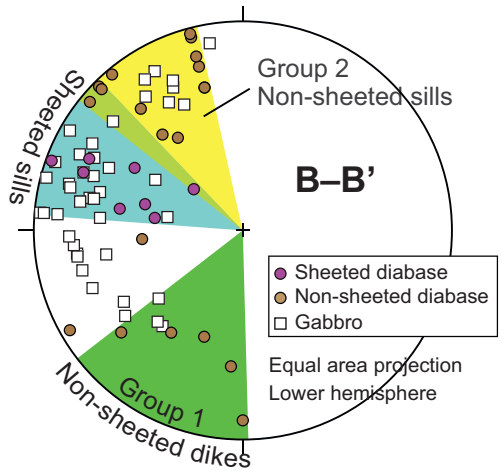


**Figure 6.** Equal-area projections (lower hemisphere) of strikes of gabbro foliations and injection planes of diabase sills/dikes in the B-B′ section. Non-sheeted diabases could be subdivided into two groups, based on their orientations. See the text for details.

Calcium ($^{43}Ca$) was used as an internal standard, and the raw data were reduced using the GLITTER 4.0 program.

### 4.3. Oxygen and Hydrogen Isotope Analyses

Oxygen isotope analysis was conducted by conventional $BrF_5$ extraction method of Clayton & Mayeda (1963) in Beijing Createch Testing Technology Co., Ltd., Beijing, China. Before analysis, whole-rock and amphibole powders (200 mesh) were heated in an oven at 105°C for 12 h. Suitable amounts of sample powders were reacted with $BrF_5$ in nickel reaction vessels under vacuum at 550°C, which converted $O_2$ to $CO_2$ by 5 Å molecular sieve carbon rods. Oxygen isotope ratios were measured on a Thermo Fisher Scientific 253 plus chromatography mass spectrometer. Analytical results for NBS 28 quartz standard have a standard deviation for $\delta^{18}O_{VSMOW}$ better than ±0.2‰.

Hydrogen isotope was measured using the method of Gong et al. (2007) in Beijing Createch Testing Technology Co., Ltd. Amphibole powders were heated under vacuum at 90°C for 12 h to remove surface water. These powders were then sealed in a quartz tube with Zn metal at 1380°C to generate $H_2$ by reacting with glass carbon. $H_2$ gas was then transferred by pure $N_2$ (150 ml/min) through chromatographic column (50°C) to a Thermo Fisher Scientific 253 plus chromatography mass spectrometer for analysis. USGS57 Biotite and USGS58 muscovite were measured as standard, yielding a standard deviation for $\delta D_{VSMOW}$ better than ±1‰.

## 5. Analytical Results

### 5.1. Whole-Rock Major and Trace Element Compositions

Whole-rock major element compositions of 200 in situ samples from the Jiding massif are listed in Table S1 (http://dx.doi.org/10.17632/x9fndtgn49.4). These samples include (1) dikes and sills of amphibolite, deformed gabbro, and diabase in the mantle unit, (2) gabbros in the lower crust, (3) diabase dikes and sills crosscutting or overlying the lower crustal gabbros, and (4) pillow lavas. In the A-A′ section, 10 foliated gabbro and amphibolite samples, as dikes/blocks cutting serpentinites, show relatively homogeneous compositions, with Mg# [$100 \times Mg/(Mg + Fe^{2+})$] of 54–63, $TiO_2$ of 1.0–1.8 wt %, and MgO of 6.7–9.3 wt %. They are variably altered with LOI mainly of 2.5–4.6 wt %.

In the B-B′ section, the gabbros in the lower crust have close Mg# and $TiO_2$, mostly in the range of 75–81 and 0.1–0.4 wt %, respectively. Only six disseminated oxide gabbros in the high-level of lower crust show variably lower Mg# (54–74) and higher $TiO_2$ content (0.5–1.3 wt %) (Figure 7). One amphibolite sample in the mantle peridotite (18JD100 in Table S1) has Mg# of 54, MgO of 6.8 wt %, and $TiO_2$ of 1.5 wt %, which is compositionally distinguishable from the lower crustal gabbros (Figure 7). Non-sheeted, discrete diabase sills/dikes in both mantle and lower crust show homogeneous compositions. Twenty-nine out of 30 analyses for these diabases contain 6.0–8.0 wt % MgO and 0.8–1.4 wt % $TiO_2$, and have Mg# of 52–64; only one sample (18JD153) shows higher Mg# of 73 and lower $TiO_2$ content of 0.3 wt %, which are comparable to the composition of lower crustal gabbros (Figure 7). Notably, there are no significant compositionally differences between diabase sills and dikes, except for the sample 18JD153. In contrast, those diabases in the sheeted sill complex show relatively heterogeneous compositions, with Mg# of 32–66, and $TiO_2$ of 0.7–1.7 wt %. Although most of these samples are compositionally similar to the non-sheeted diabases, six out of 31 analyses have lower Mg# and higher $TiO_2$ with respect to the other samples (Figure 7). On the other hand, it is notable that pillow lavas also have heterogeneous compositions (Mg# = 46–66, and $TiO_2$ = 0.5–1.7 wt %) that are in the same range with those diabases in the sheeted sill complex (Figure 7).

Most samples in the C-C′ section have Mg# of 40–66, and $TiO_2$ content of 0.7–1.8 wt %, which are comparable to the diabases and basalts in the B-B′ section (Table S1). Two samples (18JD04 and 18JD07), however,

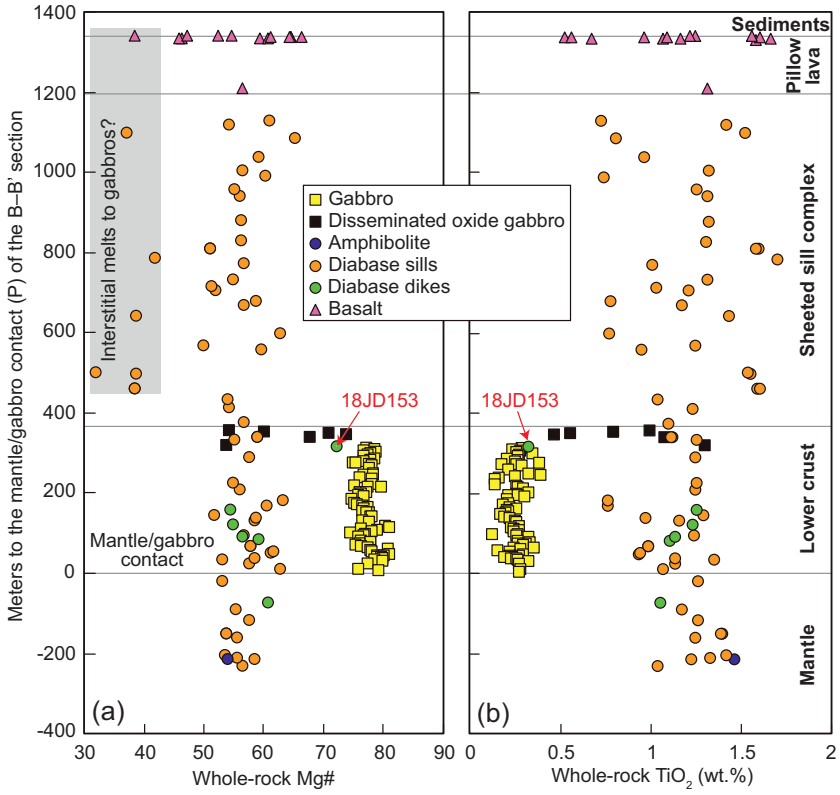


**Figure 7.** Whole-rock Mg# and $TiO_2$ (recalculated to anhydrous condition) up-section variations of the mafic rocks in the B-B′ section of the Jiding massif.

show high Mg# (83–85) and lower $TiO_2$ (0.1–0.2 wt %), which are close to the lower crustal gabbros in the B-B′ section.

Whole-rock trace element compositions of the gabbroic rocks in the P-P′ section are presented in Table S2. These gabbroic rocks include six oxide-bearing gabbros, 1 olivine gabbro, 1 gabbronorite, and the others are gabbros. The oxide-free gabbros show homogeneous chondrite-normalized rare earth element (REE) patterns, with light REE (LREE) depletion [$(La/Sm)_N$ = 0.2–0.8; N means normalization to CI chondrite, Sun & McDonough, 1989], and nearly flat middle to heavy REE (MREE and HREE) [$(Gd/Yb)_N$ mostly in the range of 0.8–1.1] (Figure 12b). All of them have moderate to strong positive Eu anomalies [δEu = 1.0–3.8; $\delta Eu = Eu_N/(Sm_N \times Gd_N)^{1/2}$]. In contrast, disseminated oxide gabbros show slightly weaker LREE depletion [$(La/Sm)_N$ = 0.3–0.4] and variable positive Eu anomalies (δEu = 1.3–1.6). In general, REE contents of gabbros are much lower than those of disseminated oxide gabbros, which in turn are also lower than or comparable to the most primitive end of Jiding diabases and basalts (data from Liu et al., 2020) (Figure 12b).

### 5.2. Mineral Major and Trace Element Compositions

Major element compositions of clinopyroxene, plagioclase, ilmenite, and amphibole from diabases, foliated gabbros, and amphibolites are listed in Table S3 and S4. All diabases are from the P-P′ lower crustal section, and the foliated gabbros and amphibolites occur as dikes or blocks in the serpentinites of A-A′ section.

Clinopyroxenes in the lower crustal diabases have homogeneous compositions, with 0.03–1.1 wt % $Cr_2O_3$, 0.3–0.8 wt % $TiO_2$, and Mg# of 77–87. They range from diopside to augite in composition (Figure 8a). In contrast, clinopyroxenes in the foliated gabbros and amphibolites also show homogeneous compositions, but with lower $Cr_2O_3$ (0–0.06 wt %), $TiO_2$ (0.2–0.3 wt %), and Mg# (66–71) with respect to the diabases. They are mainly augite in composition (Figure 8a).

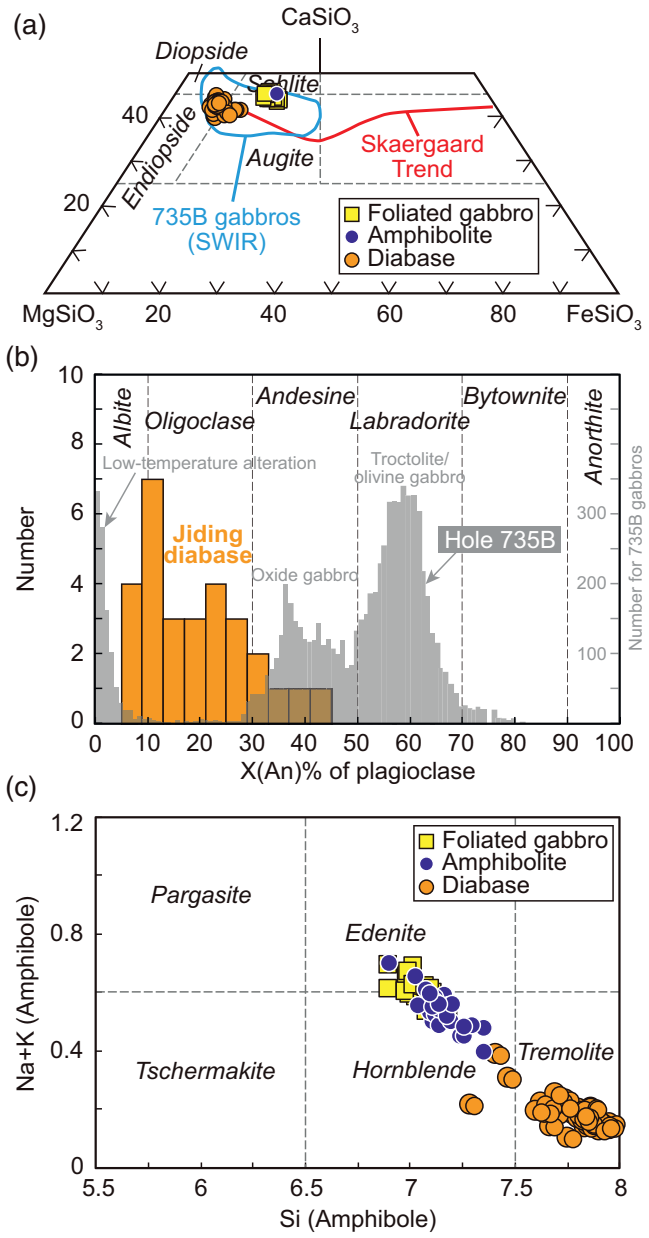


**Figure 8.** Mineral classification diagrams of clinopyroxene, plagioclase, and amphibole in the diabases from the P-P′ section, and in the foliated gabbros and amphibolites from the A-A′ section. (a) Clinopyroxene quadrilateral plot. The fileds for Hole 735B gabbros of the SW Indian Ridge (SWIR) and the Skaergaard trend are after Dick et al. (2002). (b) Histogram of plagioclase compositions in terms of anorthite fractions [$X_{An}$ = 100 × Ca/(Ca + Na + K)]. Note that only the plagioclase compositions from diabases are presented here; while the plagioclases in foliated gabbros and amphibolites are intensely altered. Data of Hole 735B gabbros are after Dick et al. (2002). (c) Alkali cations in A site versus Si in amphiboles.

The compositions of plagioclases in the diabases are relatively heterogeneous, with anorthite [An; 100 × Ca/(Ca + Na + K)] contents ranging from 6 to 44 (Table S3), which plotted in the transitional composition between disseminated oxide gabbros and low-T altered rocks, defined by large dataset of the Hole 735B gabbro section from the Atlantis Bank (Dick et al., 2002) (Figure 8b). Ilmenites in the Jiding diabases are homogeneous in composition, containing 43.7–54.7 wt % $TiO_2$, and 41.8–48.1 wt % FeO (Table S3).

Amphiboles in the Jiding diabases contain 10.1–12.5 wt % CaO, with Na in M4 site of 0.09–0.36 (Table S4), most of which show a calcic nature (calcic amphibole having CaO > 10 wt % and Na in M4 site <~0.33; Coogan et al., 2001; Manning et al., 1996). They show relatively high Si (7.31–7.99 in atomic cation), but low (Na + K) (0.10–0.39) (Table S4), mostly plotting in the tremolite field in the (Na + K) versus Si classification (Figure 8c). Only 6 out of 37 analyses show a hornblende composition. These amphiboles all have quite low F that is below the detection limits of analysis, but contain relatively high Cl contents of 0.01–0.08 wt % (Table S4). Amphiboles in the foliated gabbros and amphibolites are similar in composition to each other, but both are different from those in the diabases. They contain 10.4–11.2 wt % CaO, with Na in M4 site of 0.39–0.69 (Table S4). They have relatively lower Si (6.89–7.36 in atomic cation) and higher (Na + K) (0.40–0.71), showing an edenite–hornblende composition (Figure 8c). The Cl contents (0.05–0.2 wt %) in these amphibolies are relatively higher than those in the diabases, though their F contents are also blow the detection limits (Table S4).

As for its trace elements (Table S5), clinopyroxene in the Jiding gabbros has CI chondrite-normalized REE patterns with LREE depletion, nearly flat HREE, and weak to negligible negative Eu anomalies, which are virtually identical to clinopyroxene REE patterns in the more primitive Atlantis Bank gabbros (IODP Hole U1473A; Dick et al., 2019a; Figure 9a). They contain homogeneous trace element concentrations, with significant depletions in Sr, Zr, and Hf, and weak negative Ti anomalies, when normalized to primitive mantle (Figure 9b).

### 5.3. Whole-Rock and Amphibole H-O Isotopic Compositions

Whole-rock and amphibole H-O isotopic compositions of gabbros and diabases in the Jiding P-P′ lower crustal section are listed in Table S6. Gabbros, disseminated oxide gabbros, and diabases have homogeneous whole-rock oxygen isotopic compositions, with $\delta^{18}O_{VSMOW}$ of 8.6–11.9‰, which are much higher than that of the primary MORB (mid-ocean ridge basalt) ($\delta^{18}O = 5.7 \pm 0.3$‰; Harmon & Hoefs, 1995; Muehlenbachs & Clayton, 1972) (Table S6 and Figure 10a). In contrast, amphiboles in the diabases have $\delta^{18}O$ values ranging from 3.2‰ to 5.9‰, with 6 out of 13 samples showing $\delta^{18}O$ values lower than primary MORB (Table S6 and Figure 10a). Collectively, whole-rock and amphibole oxygen isotope analytical results in this study for the lower crust of the Xigaze ophiolite are consistent with the results reported by Agrinier et al. (1988).

Twelve out of 13 hydrogen isotopic analyses for amphibole separates of the diabases in the Jiding lower crust have homogeneous δD values of −66 to −78‰, only one sample has relatively higher δD value of −55‰ (Table S6). Our results are in a range similar to the whole-rock hydrogen isotopic compositions of gabbros in the Xigaze ophiolite reported by Agrinier et al. (1988), but with more samples having lower δD values (Figure 10b). Analytical results from our study and Agrinier et al. (1988) plot in a range between the sources

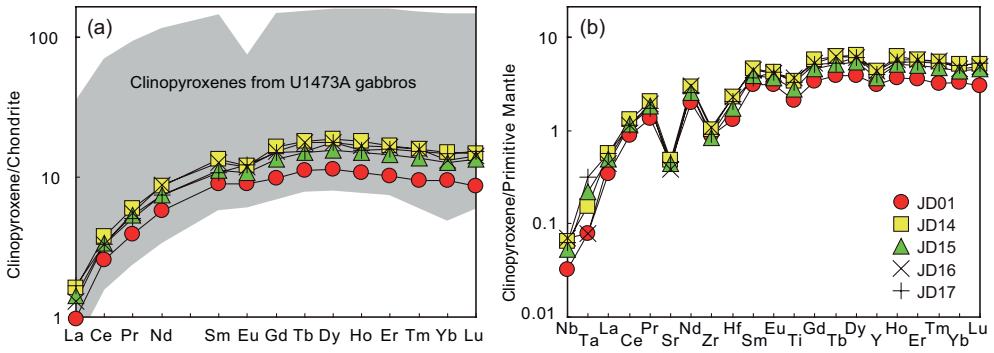


**Figure 9.** Clinopyroxene trace element compositions of representative Jiding G-series gabbros. (a) CI chondrite-normalized rare earth element patterns; (b) primitive mantle-normalized multi-element spidergrams. Data of CI chondrite and primitive mantle are from Sun and McDonough (1989). The field for clinopyroxenes from the IODP Hole U1473A gabbroic rocks at the Atlantis Bank, SW Indian Ridge is after Dick et al. (2019a).

of magmatic water (Taylor & Sheppard, 1986) and seawater metamorphism (after Alt & Bach, 2006) (Figure 10b), suggesting a mixing nature of magmatic water and seawater hydrothermal fluids.

## 6. Discussion

### 6.1. Lithological and Compositional Diversities in the Lower Crust of Xigaze Ophiolite

The P-P′ lower crustal section of the Jiding massif in the Xigaze ophiolite shows large lithological and compositional diversities, with three different rock types, i.e., gabbro, disseminated oxide gabbro, and diabase.

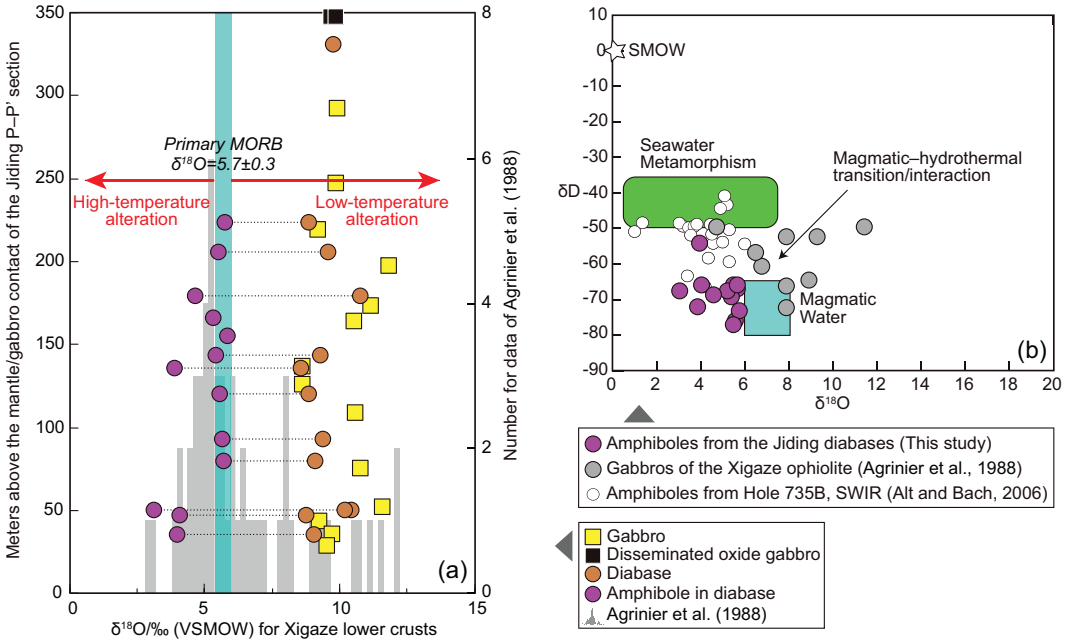


**Figure 10.** (a) Whole-rock and amphibole oxygen isotope profiles for the gabbros and diabases of the P-P′ section of the Jiding massif. (b) Amphibole oxygen and hydrogen isotopic compositions of the diabases of the P-P′ section. Data of Agrinier et al. (1988) for the Xigaze ophiolite is also added for comparison. The H-O isotopic data of the Hole 735B section at the SW Indian Ridge are from Alt & Bach (2006). The oxygen isotopic composition of primary MORB is after Harmon & Hoefs (1995) and Muehlenbachs & Clayton (1972). Black dotted lines in panel (a) link amphibole and whole-rock O isotopic analyses for individual sample. The fields of seawater metamorphism and magmatic water in panel (b) are after Alt & Bach (2006) and Taylor & Sheppard (1986), respectively. Our data overlap the fields of seawater metamorphism and magmatic water, indicating magmatic-hydrothermal transition and interaction.

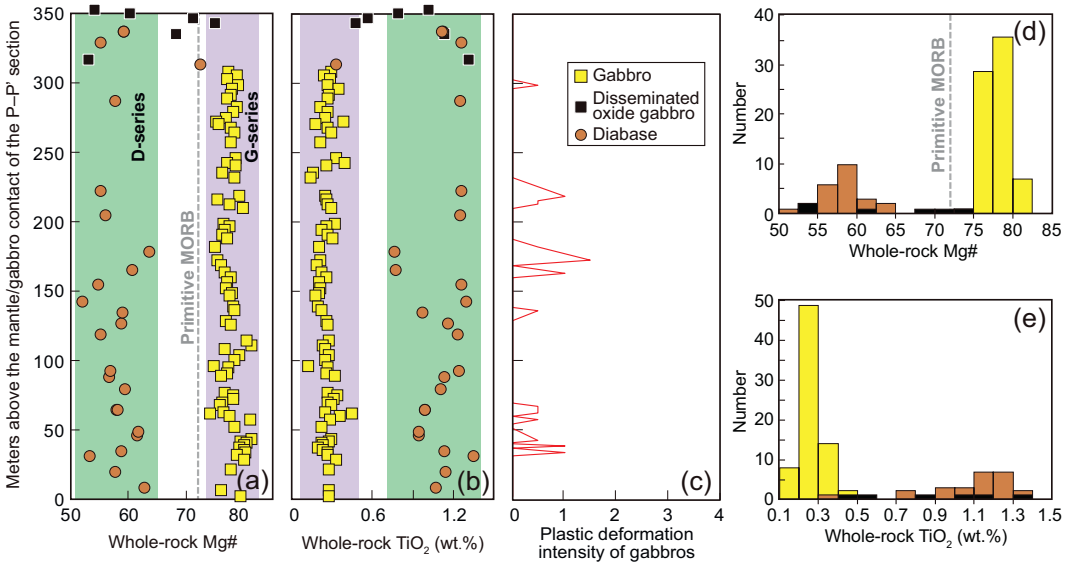


**Figure 11.** Up-section cryptic chemical variations of the gabbroic rocks and diabases above the mantle/gabbro contact of the P-P′ lower crustal section of the Jiding massif. (a, b) Whole-rock Mg# and $TiO_2$ (recalculated to anhydrous condition) stratigraphies showing the G-series gabbros, and D-series diabases and disseminated oxide gabbros, see the text for details. (c) Plastic deformation intensity of the gabbroic rocks. Deformation grades are after Dick et al. (2019b), from 0—not visible in hand specimen, to 1—deformation evident but lacking well-developed foliations, 2—clearly foliated, 3—strongly foliated (protomylonite), and 4—strongly laminated with porphyroclasts and recrystallized fine-grained neoblasts (mylonite). (d, e) Whole-rock Mg# and $TiO_2$ histograms for the gabbroic rocks and diabases in the P-P′ section. The composition of primary MORB with Mg# of ~72 is after Kinzler & Grove (1993).

In its cryptic chemical stratigraphies (Figures 11a and 11b), two compositionally distinguishable series are clearly shown, i.e., (1) relatively more primitive gabbros (termed G-series hereafter), and (2) more evolved diabases and disseminated oxide gabbros (termed D-series hereafter), although the proportion of disseminated oxide gabbros is quite low.

The G-series gabbros have higher Mg# (~75–81) relative to the recommended primary melt after ~10% melting of a MORB mantle source (Mg# = ~72; Kinzler & Grove, 1993). They also show chondritic REE abundances, and marked positive Eu anomalies (Figure 12b), indicative of a cumulative origin. In terms of whole-rock major elements, the G-series gabbros are more homogeneous than abyssal gabbros at modern slow-spreading and ultraslow-spreading ridges (Figure 12a). Notably, their compositions do not extend to the more extreme Fe-rich and Mg-rich compositions, seen, respectively, in Hole U1473A at the Atlantis Bank of SW Indian Ridge (SWIR), and Hole U1309D at the Atlantis Massif of Mid-Atlantic Ridge (MAR). In terms of whole-rock trace elements, the G-series gabbros are comparable to the gabbros/gabbronorites at the Atlantis Massif, but have higher REE abundances than its primitive (olivine-rich) troctolites (Figure 12b). Therefore, the lack of the Mg-rich (primitive) compositions for the Jiding G-series gabbros indicates on one hand that their parental melts are more evolved than those for the Atlantis Massif troctolites, hence resulting in the predominant crystallization of plagioclase and clinopyroxene in the system, but not of olivine. This is also evidenced by the bulk composition estimates for the Jiding gabbroic rocks (Liu et al., 2018), which have lower bulk Mg# (~76) and higher bulk $TiO_2$ (0.4 wt %) than the Atlantis Massif troctolites, i.e., mean Mg# and $TiO_2$ are 86 and 0.1 wt %, respectively ($N = 11$; Godard et al., 2009). On the other hand, it also indicates that there was no interaction or hybridization of mantle rocks involved in their crystallization, which was different from the intense melt-rock interactions between MORB-type melts and mantle peridotites, generating the olivine-rich troctolites at the Atlantis Massif (e.g., Drouin et al., 2009; Godard et al., 2009; Suhr et al., 2008).

Another notable feature is the predominance of gabbro over olivine gabbro in the G-series, as is also seen for the gabbroic drill cores at the Atlantis Massif (Godard et al., 2009; Ildefonse et al., 2007), but not at the Atlantis Bank (Dick et al., 2019b) (see the compilation in Figure 13). It should be noted that clinopyroxenes in the Jiding G-series gabbros have REE contents that are comparable to the more primitive

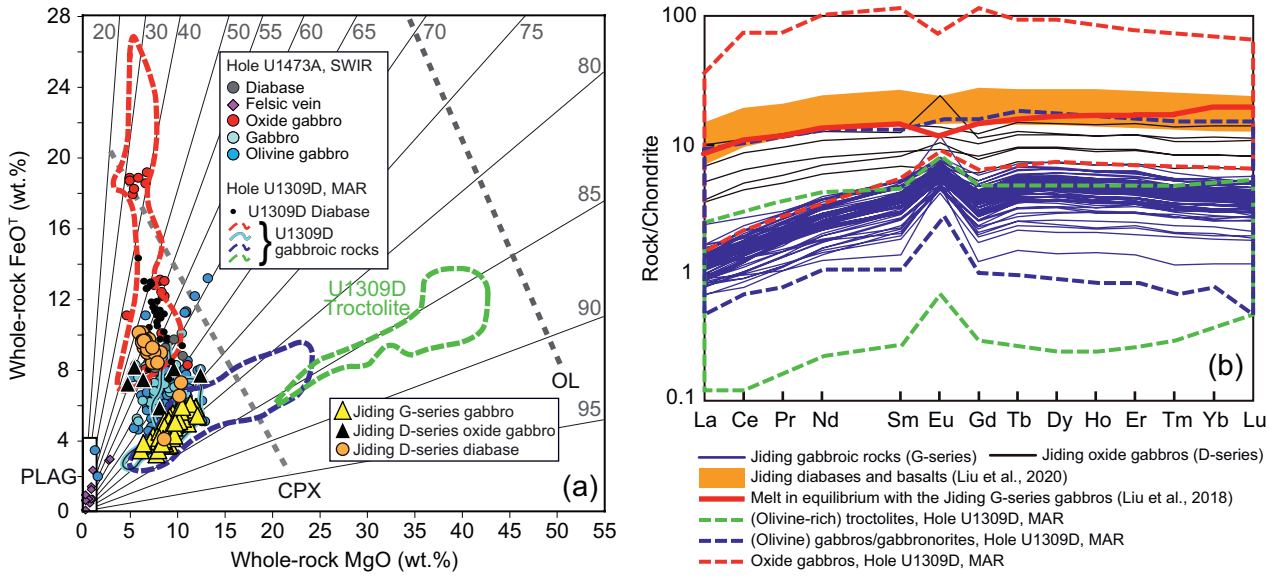


**Figure 12.** (a) Whole-rock FeO$^T$ versus MgO (recalculated to anhydrous condition) for the P-P′ lower crustal gabbroic rocks and diabases. Fields for the Atlantis Massif Hole U1309D (Mid-Atlantic Ridge) are after Godard et al. (2009). Data for the Atlantis Bank Hole U1473A gabbros (SW Indian Ridge) are after Dick et al. (2019b). Thin black lines indicate constant Mg# ranging from 20 to 95. Variations of Fe-Mg compositions for olivine (OL), clinopyroxene (CPX) and plagioclase (PLAG) in U1309D gabbros are represented by thick dashed lines (OL, CPX) and a white rectangle (PLAG). (b) Whole-rock CI chondrite-normalized rare earth element (REE) patterns for the P-P′ lower crustal gabbroic rocks. REE data of the Jiding diabases and basalts and the melt in equilibrium with the G-series gabbros from Liu et al. (2018, 2020) are also added for comparison. Compositional fields for the gabbroic rocks from Hole U1309D at the Atlantis Massif of Mid-Atlantic Ridge are after Godard et al. (2009).

clinopyroxenes from the Hole U1473A gabbros at the Atlantis Bank (Figure 9a; Dick et al., 2019a). This indicates that the G-series gabbros are relatively more primitive than the average Atlantis Bank gabbros. Therefore, considering the overall primitive character of the Jiding gabbros, the predominance of gabbro over olivine gabbro can likely be attributed to a high percentage of late melt retention reacting out modal olivine (Dick et al., 2019b). The retention of interstitial melts in the crystal mush has been suggested to be associated with the degree of ductile deformation in response to tectonic shearing of detachment faults (Sanfilippo et al., 2019). It is obvious that gabbros from Jiding (Figure 11c in this study) and Atlantis Massif (Ildefonse et al., 2007) both show much weaker crystal-plastic deformations (deformation intensities are 0–1 and 0–2, respectively) than the Atlantis Bank gabbros (deformation intensity is up to 4; Ildefonse et al., 2007), hence confirming weaker overall ductile deformations for Jiding and Atlantis Massif. This would result in the retention of relatively larger amounts of interstitial, evolved melts in the crystal mush at Jiding and Atlantis Massif than at the Atlantis Bank. Lack of intense ductile deformation in Jiding and Atlantis Massif suggests that the deformation of gabbros occurred mainly in the brittle deformation regime, while the ductile deformation was localized dominantly in the deep. Therefore, we speculate that the characteristics of the Jiding G-series gabbros, including their fine grain sizes, argue for fairly rapid uniform cooling in a relatively cold crust at the time of emplacement, consistent with infrequent intrusion and a low magma supply. This condition is quite different from the relatively large amounts of magma supply occurred at the Atlantis Bank, where both compaction-driven and deformation-driven interstitial melt migration happened, resulting in large diversities of its lower crustal lithologies (Zhang et al., 2020).

Relative to the G-series gabbros, the D-series disseminated oxide gabbros show heterogeneous compositions, with variably lower whole-rock Mg# and higher $TiO_2$ content (Figures 11a, 11b, 11d, and 11e). Besides, these disseminated oxide gabbros have higher REE abundances, and most of them show weak to negligible Eu anomalies, which are comparable to the oxide gabbros at the Atlantis Massif (Figure 12b). These features indicate that the disseminated oxide gabbros formed by in situ crystallization of variably evolved melts. This is consistent with the limited FeO enrichment presented in them (Figure 12a). Besides, these disseminated oxide gabbros have REE abundances that are comparable to the melt in equilibrium with the G-series gabbros (Figure 12b; Liu et al., 2018). It implies that the melts from which the disseminat-

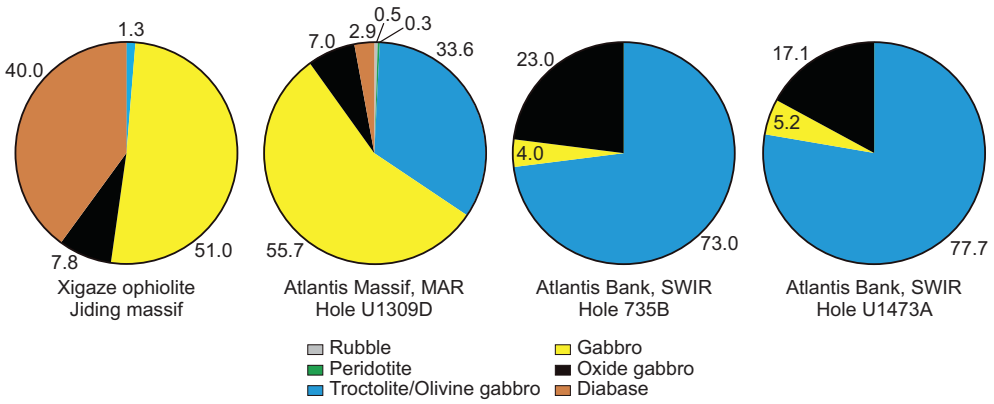


**Figure 13.** Lithology proportions (in percent) of representative gabbroic sections from the Jiding massif, Xigaze ophiolite (this study), Hole U1309D at the Atlantis Massif, Mid-Atlantic Ridge (MAR) (Blackman et al., 2006), and Hole 735B and U1473A at the Atlantis Bank, SW Indian Ridge (SWIR) (MacLeod et al., 2017).

ed oxide gabbros were derived are likely interstitial to the crystal mush, after variable extents of fractional crystallization. The D-series diabases, on the other hand, also show homogeneous compositions, but have much lower whole-rock Mg# and higher $TiO_2$ content than the G-series gabbros (Figures 11a, 11b, 11d, and 11e). Besides, in terms of whole-rock major elements, most of these diabases contain much higher $FeO^T$ contents than the G-series gabbros, and are comparable to the diabases from IODP Hole U1473A at SWIR and U1309D at MAR (Figure 12a). In terms of whole-rock trace elements, the D-series diabases have suprachondritic REE abundances, and lack Eu anomalies (Figure 12b). These features collectively suggest that the D-series diabases are derived from in situ crystallization of melts. These melts must have experienced variable differentiation, hence have a more evolved character than the recommended primary MORB (Kinzler & Grove, 1993). The D-series diabases have $(La/Sm)_N$ ratios (averaged at ~0.52; data from Liu et al., 2020) that are systematically higher than those of the G-series gabbros (averaged at ~0.35; Table S2). This distinction is also shown by the relatively steeper LREE trends in the G-series gabbros with respect to the D-series diabases (Figure 12b). A relatively higher $(La/Sm)_N$ ratio implies that olivine and clinopyroxene were dominant phases in the source of the D-series diabases, because plagioclase crystallization would lower the $(La/Sm)_N$ ratio of the system (e.g., Zhang et al., 2020). However, petrographic observations show that clinopyroxenes in the G-series gabbros commonly occur as oikocrysts or interstitial to plagiolcases (Figure 5d), confirming an early crystallization of plagioclase than clinopyroxene. Therefore, the distinct mineral crystallization orders of the parental melts for the D-series diabases and G-series gabbros imply that they are not genetically linked. It should be noted, on the other hand, that the diabases in the sheeted sill complex and pillow lavas show larger compositional variations than those diabases in the lower crust and mantle. Six diabases and one basalt show markedly lower whole-rock Mg# than the others (Figure 7a). This compositional dispersion in the sheeted sill complex and pillow lavas could be explained by that the more evolved samples were generated by interstitial melts to the cumulates, which were compacted from the crystal mush and fed the upper crust. Nevertheless, the expulsion of these interstitial melts is quite limited, and most of the upper crustal rocks show compositions that resemble those in modern oceans (Figure 12a).

In the lower crust, disseminated oxide gabbros and diabases are seen not only in the Jiding massif of the Xigaze ophiolite, but also in abyssal gabbro sections such as Hole 735B and U1473A at the Atlantis Bank (e.g., Dick et al., 2002, 2019a, 2019b; MacLeod et al., 2017), and Hole U1309D at the Atlantis Massif (Blackman et al., 2006; Godard et al., 2009). For example, the 735B section contains large amounts of oxide-rich gabbros through the whole section. These oxide-rich gabbros contain higher $FeO^T$ and $TiO_2$ contents than the ambient oxide-poor olivine gabbros and troctolites (Dick et al., 2002), a character similar to the Jiding massif. The oxide-rich gabbros in Hole 735B crop out spatially close to regional ductile shear zones, which may be controlled by the activities of oceanic detachment faults. Therefore, the migration of evolved melts through the 735B section was interpreted to be accounted for by tectonic-controlled melt expulsion (e.g., Dick et al., 2002; Zhang et al., 2020). However, the Jiding lower crust is different from the Atlantis Bank, because disseminated oxide gabbros in the former occur only at the top, but not throughout the section, as

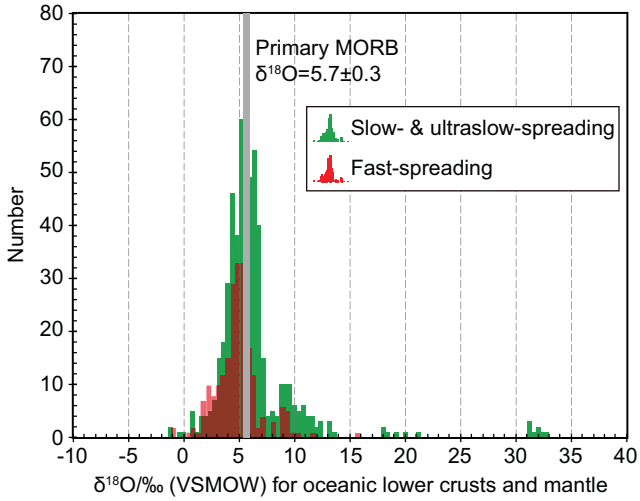


**Figure 14.** A global compilation of oxygen isotopic compositions of oceanic lower crusts and upper mantle in modern oceans and ophiolites. Slow-spreading and ultraslow-spreading environments include the Xigaze ophiolite, Ligurian ophiolite, and the Hole 735B at the SW Indian Ridge. Fast-spreading environments include the Hess Deep at the East Pacific Rise, and the Oman ophiolite. The data and references are presented in Table S7.

is shown in the Atlantis Bank. This implies that the migration of such evolved melts were limited and localized in the Jiding lower crust. This is consistent with the retention of relatively large amounts of interstitial melts in the Jiding crystal mush and its cold lower crust, as discussed above. Due to the lower wall-rock temperature of the Jiding oceanic crust with respect to Atlantis Bank and Atlantis Massif, the crystal grain size is much small for the G-series gabbros (~1–2 mm; Figures 5c and 5d), the plastic deformation is weaker for both the G-series gabbros and D-series disseminated oxide gabbros (Figure 11c), and the total magma supply is quite lower (~350-m thick lower crust in Jiding relative to >1.5-km thick at Atlantis Bank, and ~1.4-km thick at Atlantis Massif; Dick et al., 2002; Godard et al., 2009).

On the other hand, although diabase indeed exists in the gabbroic drill cores at Atlantis Bank and Atlantis Massif, its proportions in these two sections are quite low. For example, diabases cover only 2.9% in the Hole U1309D at the Atlantis Massif (Blackman et al., 2006), and even are rarely seen in Hole 735B and U1473A at the Atlantis Bank (MacLeod et al., 2017) (as shown in Figure 13). In contrast, diabases constitute ~40% of the Jiding lower crustal section (Figure 13). The lithological proportional distinction between these three regions indicates that much larger amounts of melts must have occurred in the Jiding lower crust for the generation of diabases, though its total magma supply is the lowest. Field observations clearly show that, in the Jiding lower crust, the D-series diabases cut both the G-series gabbros and D-series disseminated oxide gabbros (e.g., Figures 3 and 4). This confirms that the diabases are the latest-stage melt products with respect to the gabbros and disseminated oxide gabbros. It should be noted that diabase is commonly generated in a much shallower level than gabbroic rocks, because of its smaller grain size (Liu et al., 2016). This implies that these gabbroic rocks should have been exhumed to a shallower level, before the melts intruded and generated diabase dikes and sills. Moreover, fresh diabase dikes/sills with chilled margins are also found cutting intensely serpentinized mantle peridotites (Figure 4c), which suggest that the dike/sill emplacement was also later than the exhumation and low-temperature alteration (i.e., serpentinization) of mantle peridotites (Liu et al., 2016; Zhang et al., 2016). Therefore, all lines of evidence indicate that an anomalous amount of melts had fed the Jiding oceanic crust to generate these diabases, after the exhumation and pervasive low-temperature alteration of both gabbroic and mantle rocks. These late-stage melts are compositionally indistinguishable from those discrete diabase dikes in modern lower oceanic crusts (e.g., Atlantis Bank and Atlantis Massif; Figure 12a), but their amounts are much larger.

### 6.2. Intense, Pervasive Magmatic-Hydrothermal Interaction Through the Xigaze Lower Crust

The common occurrence of ilmenites in the Jiding sheeted and non-sheeted diabases indicates that these rocks were derived from Fe–Ti-rich melts, which are probably late-stage evolved melts percolating gabbros. These diabases typically contain numerous green amphiboles, some of which occur as rims or coronas of clinopyroxenes. Most of these amphiboles have low $TiO_2$ contents (<1 wt %) and F (below the detection limits), and relatively high Cl (0.01–0.08 wt %), having a tremolite affinity (Table S4 and Figure 8c). All these features indicate that these amphiboles are of hydrothermal origin (Coogan et al., 2001). We use two thermobarometers of Gerya et al. (1997) and Holland & Blundy (1994) to calculate the crystallization temperature of these amphiboles, giving results of 458–552°C ($T_G$, averagely 493°C), and 610–711°C ($T_{HB}$, averagely 645°C), respectively, and their equilibrium pressures of 144–1,821 bar (averagely ~1 kbar) (Table S4). Note that the thermometer of Holland & Blundy (1994) is established for calculating the equilibrium temperatures of amphibole–plagioclase pairs. The plagioclases in the Jiding diabases contain a large range of An contents (6–44), and plot between the oxide-rich gabbros and low-T alteration fields of the 735B section (Figure 8b). It indicates that some of these plagioclases with relatively low An contents are secondary products recrystallized during interaction with hydrothermal fluids (Manning et al., 1996), mak-

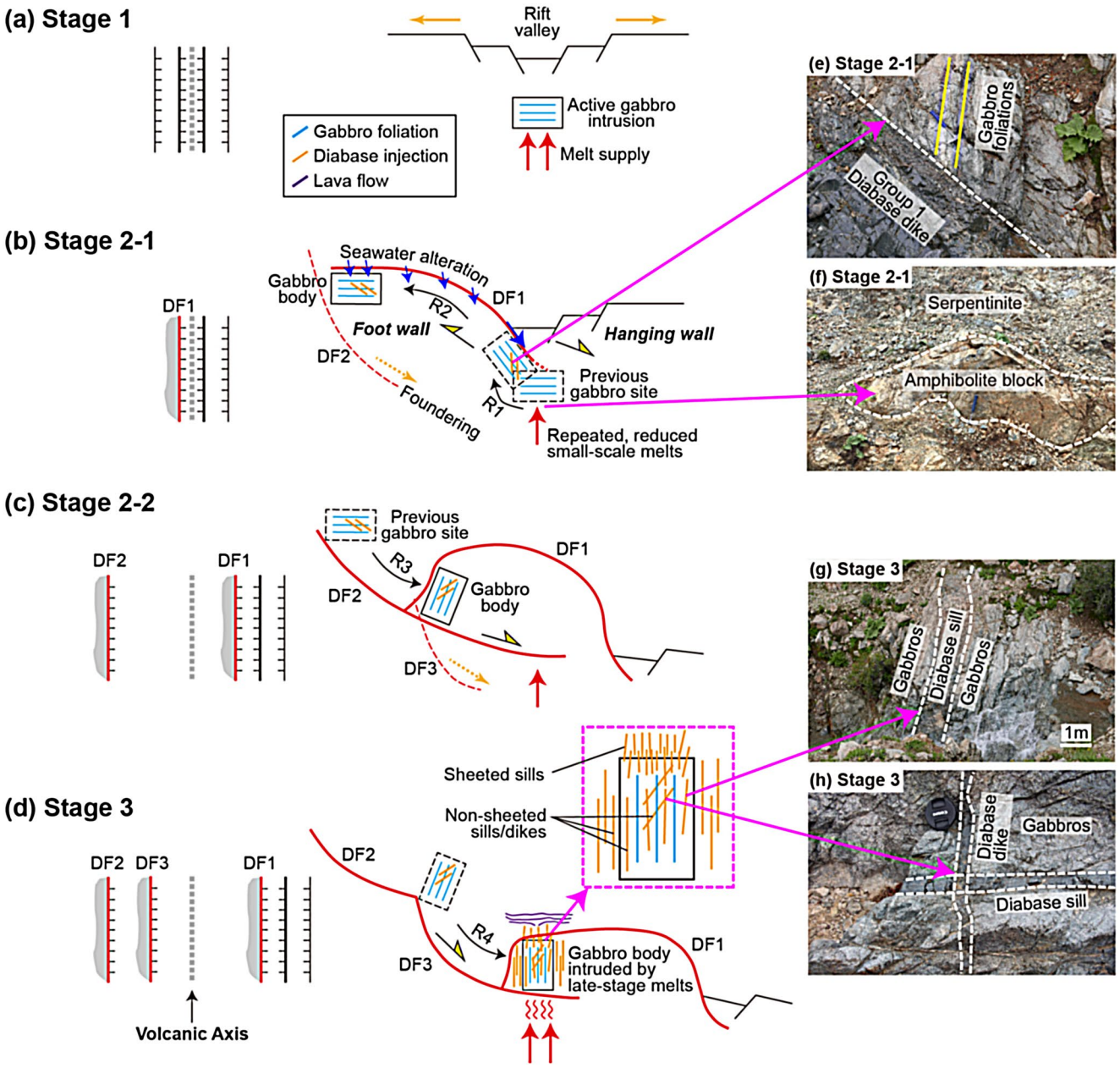


**Figure 15.** A proposed model for the generation of sheeted and non-sheeted "pseudosills" in the Xigaze ophiolite. The crustal architectures are shown in a top view version in the left, and a cross-section view version in the right, respectively. See the text for details. DF: detachment fault, R: rotation.

ing $T_{HB}$ calculations misleading to some extent. Thus, we suggest that the crystallization temperatures of these green amphiboles are in the range of ~450°C–550°C, which are much lower than that of magmatic amphiboles (>700°C), but much higher than that of late-stage low-temperature alterations forming clays, carbonates, zeolites, or prehnites (<250°C) (Alt & Bach, 2006).

Amphibole compositions and equilibrium temperatures/pressures suggest that the Jiding D-series diabases formed by crystallization of evolved melts that interacted with hydrothermal fluids. H-O isotopic data for these amphiboles clearly show a mixed metasomatic source of magmatic water and seawater hydrothermal fluids, suggesting magmatic-hydrothermal transition and interaction (Figure 10b). During the emplacement of these diabases, the wall-rock temperature was not quite low (~450°C–550°C), and the gabbros were still hot, but in a brittle deformation regime, forming curved or branched contacts between diabases and

gabbros (Figures 4g and 4h). This is also evidenced by the close crystallization ages between the diabases and gabbros (see the review by Liu et al. (2016)). Thus, the gabbros experienced a rapid exhumation during their formation, and then were intruded by evolved, Fe–Ti-rich melts, along with seawater hydrothermal circulation, forming the ilmenite-bearing and green amphibole-bearing diabases. This suggests a rapid magmatic-hydrothermal transition and intense interaction, characterizing the lower crustal accretion of the Xigaze ophiolite.

### 6.3. Evidence for the Occurrence and Location of Detachment Faults in the Xigaze Ophiolite

The Xigaze ophiolite has been suggested by previous studies to form at a slow-spreading to ultraslow-spreading ridge, based on its anomalously thin oceanic crusts (e.g., Girardeau et al. 1985a; Liu et al., 2016, 2018; Nicolas et al., 1981; Wu et al., 2014). At (ultra)slow-spreading ridges, the magma supply is commonly quite low and episodic (e.g., Dick et al., 2002, 2019b), and ocean spreading is modeled to be accommodated by tectonic extension (i.e., oceanic detachment faulting) (Tucholke et al., 2008). Previous studies have provided paleomagnetic and structural evidence for the occurrence of detachment fault in the Xigaze ophiolite, but its location in this region is still poorly constrained. For example, paleomagnetic data for the Xigaze sheeted sills and mantle-hosted mafic dikes have revealed large internal block rotations, which were attributed to footwall rotations during detachment-fault-controlled exhumation (Maffione et al., 2015). Besides, structural studies during recent 1:50,000 geological mapping have identified mylonitic serpentinite belts in both the northern and southern parts of the Xigaze ophiolite (Li et al., 2016). Notably, strongly foliated gabbros and amphibolites were found, as dikes or blocks in the serpentinized mantle peridotites, which were explained to be generated by ductile shearing at amphibolite-facies conditions (Li et al., 2016).

Our study has identified a rapid exhumation experienced by the gabbroic rocks during or just after their formation, along with seawater hydrothermal alteration and magmatic-hydrothermal interaction. Oxygen isotopic analysis in this study for the amphiboles in the Jiding D-series diabases shows MORB-like to relatively depleted $\delta^{18}O$ values (Figure 10a), suggesting that some of these amphiboles were involved in moderate-temperature to high-temperature hydrothermal alterations during their formation. In comparison, whole-rock analysis for all D-series diabases gives enriched $\delta^{18}O$ values of 8.6–10.8‰ with respect to primary MORB, even for those samples containing amphiboles with depleted $\delta^{18}O$ (Figure 10a). Besides, the G-series gabbros have $\delta^{18}O$ values (8.7–11.9‰) that are in the same range with the D-series diabases. This shows a clear O isotopic contrast between amphibole and whole-rock analyses, most likely due to the influence of low-temperature alteration minerals of both diabases and gabbros in bulk $\delta^{18}O$. For example, plagioclases in these rocks are intensely altered into saussurite and clay (Figure 5), which would contribute largely to the elevated bulk $\delta^{18}O$ (e.g., Alt & Bach, 2006). Therefore, whole-rock analysis for these diabases and gabbros shows mixed O isotopic compositions, which are controlled by modal compositions of low-temperature alteration minerals and relative mass of rock and fluids (Alt & Bach, 2006). Nevertheless, the Xigaze lower crust shows both enriched and depleted $\delta^{18}O$ values relative to primary MORB, hence suggesting low-temperature and high-temperature seawater hydrothermal alterations, respectively. High-temperature seawater hydrothermal alterations were also identified in fast-spreading lower oceanic crusts of the EPR and Oman ophiolite, as evidenced by their depleted $\delta^{18}O$ compositions (see the compilation in Figure 14; data and references are presented in Table S7). This was ascribed to seawater injection to the uppermost lower crust through sheeted dike complex, which is the site of axial melt lens, or was accounted for by the elevated water contents of evolved melts (Stakes & Taylor, 1992). However, low-temperature seawater alterations, which form enriched $\delta^{18}O$, have rarely been reported for fast-spreading lower oceanic crusts (Gao et al., 2006) (Figure 14). This is mainly due to the lower crustal accretions at a steady state, where the temperatures are relatively high. In contrast, enriched $\delta^{18}O$ values have been widely identified in gabbros and mantle rocks at slow-spreading and ultraslow-spreading environments (Figure 14). An interpretation is that oceanic detachment faults typical of these environments could exhume deep-seated rocks to a much shallower level or seafloor, and expose these rocks in long-term contact with seawater at low temperatures (Alt & Bach, 2006; Gao et al., 2006; Tribuzio et al., 2014). Therefore, detachment faults play a key role in seawater circulations at slow-spreading and ultraslow-spreading ridges (Escartín et al., 2008, 2017; Gao et al., 2006), forming the pervasively occurred depleted and enriched O isotopic compositions of the lower crusts, as have been identified in the Xigaze ophiolite (Figure 10a).

On the other hand, the Xigaze ophiolite is characterized by the occurrence of foliated gabbro and amphibolite dikes or blocks in the serpentinized mantle peridotites, as shown in Figures 3, 4, and S1. Petrographic observations show that these foliated gabbros and amphibolites typically contain brown amphiboles, which are metamorphosed products of clinopyroxenes (Figures 5a and 5b). These amphiboles have an edenite–hornblende composition, which is different from the hydrothermal amphiboles in the diabases (Figure 8c). Based on their major element compositions, we calculated the equilibrium temperature and pressure, using the thermobarometer of Gerya et al. (1997), for the generation of amphibolies in the foliated gabbros and amphibolies, giving homogeneous results averaged at ~580°C–590°C and 3 kbar (Table S4). P-T calculations clearly suggest that these rocks have experienced amphibolite-facies metamorphism at moderate temperature and ~10 km in depth. It should be noted that the foliated gabbros and amphibolites also show variable extents of deformations up to protomylonitic conditions (Figures 5a and 5b), hence suggesting the amphibolite-facies metamorphism was also accompanied by intense shearing. Deformed gabbros and amphibolites have been previously identified in some ophiolites and modern oceanic lithospheres. For example, mylonitic gabbros and amphibolites were reported occurring along a shear zone in the Mirdita ophiolite, Albania (Maffione et al., 2013; Nicolas et al., 1999, 2017). Besides, mylonitic oxide-rich gabbros also commonly occur in the Hole 735B and U1473A at Atlantis Bank, which are spatially associated with regional tectonic shear zones (e.g., Dick et al., 2002, 2019b). The formation of these strongly deformed gabbros and amphibolites needs syn-magmatic shearing and high-temperature metamorphism (e.g., Dick et al., 2019b). Therefore, the occurrence of foliated gabbros and amphibolites has been regarded as strong evidence for detachment faulting (Dick et al., 2002; Maffione et al., 2013; Nicolas et al., 2017), which controls the deformation, metamorphism, and alteration of oceanic lithospheres (Escartín & Canales, 2011). Direct evidence for this interpretation is the identification of amphibolite in the serpentinite/talc matrix, as one of the most dominant rock types along the detachment surface at 15°45′N, Mid-Atlantic Ridge (Escartín et al., 2003; MacLeod et al., 2002, 2011). Therefore, we argue that the foliated gabbros and amphibolites in the Xigaze ophiolite were generated by detachment faulting deeply rooted to ~10 km at ~600°C, close to the brittle-ductile transition. Moreover, field observations in this study have shown that these foliated gabbros and amphibolites occur as dikes or blocks throughout the serpentinized mantle peridotite section (e.g., A-A′ section; Figure S1). It indicates that the high-temperature deformation and metamorphism of mafic rocks were synchronous with or shortly after the low-temperature serpentinization of mantle rocks. A plausible interpretation is that mantle serpentinization occurred along the detachment surface, accompanied by seawater hydrothermal circulation from the top, and repeated melt injections from the bottom. Therefore, the detachment surface in the Xigaze ophiolite is most likely along present-day mantle serpentinization; and detachment faulting was terminated at the south of the ophiolite (as shown in Figure 2b).

### 6.4. The Role of Detachment Faults in the Generation of Sheeted and Non-sheeted Sills

As discussed above, detachment faulting may have controlled the rapid exhumation of gabbroic and mantle rocks in the Xigaze ophiolite, along with efficient seawater hydrothermal circulation and magmatic-hydrothermal interaction. Diabase sills and dikes, as the latest-stage melt products, formed just afterwards. Our structural measurements have revealed variable orientations of these diabases with respect to the gabbro and mantle foliations (Figure 6). Diabases in the sheeted sill complex have strikes mainly trending NW, which are consistent with the average magmatic foliations of gabbros (Figure 6), and the high-temperature primary mantle foliations (Girardeau et al., 1985b). Non-sheeted diabases, however, contain two groups based on their orientations. Group 1 shows diabase strikes that are mainly subperpendicular to the average gabbro foliations, hence are defined as dikes (Figure 6). In contrast, Group 2 is composed of diabases with strikes that are subparallel with the average gabbro foliations, hence occurring as "sills" (Figure 6). Dramatic orientation distinctions among all diabases are probably associated with the geometry of the gabbro body during multi-stage melt injections. Based on geological, geophysical, and numerical modeling studies, the footwall of detachment faults would commonly be rotated to variable extents during its exhumation, due to flexural unloading (e.g., Buck, 1988; Kelemen et al., 2007; Lavier et al., 1999; MacLeod et al., 2009, 2011; Maffione et al., 2013, 2015; Morris et al., 2009; Parnell-Turner et al., 2017). Besides, during or just after the evolution of detachment faulting, footwall foundering (Sauter et al., 2013) and mass wasting (Cannat et al., 2013; Escartín et al., 2017; Smith et al., 2014) due to gravity instability are commonly found as im-

portant mechanisms to reshape seafloor morphology and reduce the slope of detachment surface. These processes may have played a critical role in changing the geometry of the gabbro body at the Xigaze paleo axis through time, along with multi-stage, variable amounts of melt intrusions.

In Figure 15, we proposed a model to illustrate the dynamic crustal accretion of the Xigaze ophiolite. At the earliest stage, the Xigaze paleo ridge spreaded at a slow to ultraslow rate, in which period a series of normal faults occurred at the rift valley walls (Figure 15a, Stage 1). Beneath the rift valley, an active gabbro intrusion was generated at relatively large amounts of melt supply, and the magmatic foliation of gabbros was mainly subhorizontal, due to several processes such as mineral crystallization and segregation, and magma flow. When the magma supply waned to accommodate ~30–50% extension (as modeled by Tucholke et al., 2008), a detachment fault initiated along one of the normal faults (DF1 in Figure 15b, Stage 2-1). Gabbros and mantle peridotites were exhumed to a shallow level or even to the seafloor, where they would experience long-term seawater hydrothermal alteration, as revealed by the enriched O isotopes of gabbros (e.g., Figure 10; this study and Agrinier et al., 1988) and pervasive serpentinization of mantle peridotites. Besides, seawater could also inject into deep mantle along the detachment fault (Escartín et al., 2003; MacLeod et al., 2002, 2011). In this period, the magma supply was reduced, and only small amounts of melts intruded repeatedly into the intensely serpentinized mantle. The emplacement depth of these melts was most likely ~10 km at 600°C, as constrained by the P-T calculations for the amphibolite-facies metamorphism experienced by foliated gabbro and amphibolite dikes/blocks in the serpentinites (Figure 15f). During the exhumation, gabbros and mantle peridotites would be rotated, and their foliations tend to be oblique, when they were uplifted to the slope of the footwall (Rotation 1, R1 in Figure 15b). At this time, small amounts of melts could intrude into the gabbro body at a shallow level in the brittle deformation regime, generating the non-sheeted, discrete Group 1 diabase dikes (Figure 6, 15e). Subsequent footwall exhumation and rotation could change the geometry of the gabbro body. The second rotation (R2 in Figure 15b) of the gabbro body would result in a continuous transition of the gabbro foliations from being oblique to subhorizontal at the top of footwall.

Due to gravity instability, the footwall of detachment faults might founder along new faults initiated at its top (DF2 in Figures 15b and 15c). The gabbro body was rotated once again, and its magmatic foliations changed from being subhorizontal to oblique (R3 in Figure 15c, Stage 2-2). Continuous foundering, if it happened, resulted in the fourth rotation (R4) of the gabbro body, after which period the gabbro foliations were transformed to be subvertical (Figure 15d, Stage 3). The whole evolution of these detachment fault systems was ultimately terminated, when relatively large amounts of melts burst again at the ridge axis. These melts migrated vertically and injected into the gabbros and serpentinized mantle peridotites, generating "pseudosills," i.e., the sheeted sill complex and Group 2 non-sheeted sills (Figures 6, 15d, and 15g). These melts could also intrude into the Group 1 discrete diabase dikes, resulting in intersected diabase dikes and sills in the gabbro body (Figure 15h).

Our model shows that the gabbros and mantle peridotites of the Xigaze ophiolite, as the footwall of detachment fault, may have experienced exhumation and multi-stage rotations and foundering, before the emplacement of sheeted and non-sheeted "pseudosills." These processes suggest the important role of detachment faulting, block rotation, and foundering, along with mass wasting, in reshaping the oceanic crustal architecture, which are also well documented for modern oceanic lithospheres (e.g., Cannat et al., 2013; Escartín et al., 2017; Sauter et al., 2013; Smith et al., 2014). For example, side-scan sonar images have revealed continuous exhumations of serpentinized mantle peridotites at the eastern SWIR, where rheological changes initiated a new master fault cutting the footwall of an earlier fault (Sauter et al., 2013). Similar observations have also been documented at the Krasnov area of MAR (Cannat et al., 2013). Detachment along the new master fault would result in decreasing of the slopes of oceanic core complexes to less than 20° (Cannat et al., 2013). This implies that the relative block rotation during its foundering or mass wasting was quite large. Besides, geophysical observations on ~16.5°N at the MAR have provided evidence for multi-stage block exhumation, rotation, and mass wasting (foundering), along a series of detachment surfaces that are subparallel with the spreading axis (Smith et al., 2014). Rotations through time would change the orientations of gabbro and mantle foliations to a significant extent, a process resetting the structural relations of gabbros, diabases, and extrusive lavas. Besides, microbathymetry data and in situ observations between 13°20′N and 13°30′N at the MAR showed that mass wasting of the footwall has reduced the slope

of detachment faults, and resulted in morphologically complex chaotic terrains (Escartín et al., 2017). An alternative model, however, can also explain the generation of non-sheeted, discrete diabase dikes cutting the gabbros and mantle peridotites. At the final stage of the life cycle of oceanic core complex, the detachment fault would migrate across the ridge axis, when detachment accommodates more than half of the plate separation (i.e., MacLeod et al., 2009). New melt intrusions are then captured by the footwall of detachment faults (footwall capture model), which could explain the common occurrence of gabbros and diabases in the oceanic core complex (Blackman et al., 2006; Dick et al., 2000, 2019b; Godard et al., 2009; Ildefonse et al., 2007; MacLeod et al., 2002). In this scenario, however, the dikes in the gabbros and mantle peridotites tend to show variable orientations (Blackman et al., 2006; Godard et al., 2009), which are different from the strikingly consistent orientations between non-sheeted sills and gabbros in the Xigaze ophiolite (Figure 6).

### 6.5. Construction of Slow-Spreading and Ultraslow-Spreading Oceanic Crusts

The geometry of sheeted dike complexes at modern slow-spreading and ultraslow-spreading ridges are still poorly studied, due to the lack of in situ drill cores into the upper crusts (see the review in Karson, 2018). However, detailed field observations for those in ophiolites could provide key insight into the geometry of internal oceanic crustal architectures. To date, well-established slower-spreading type ophiolites include the Alpine-Apennine ophiolites in Italy/France (e.g., Frassi et al., 2017; Lagabrielle & Cannat, 1990; Lagabrielle et al., 2015; Manatschal et al., 2011; Sanfilippo & Tribuzio, 2011), Mirdita ophiolite in Albania (e.g., Maffione et al., 2013; Nicolas et al., 1999, 2017), Coast Range ophiolite in California (Hopson et al., 2008), and Xigaze ophiolite in Tibet, China (Girardeau et al., 1985a; Liu et al., 2018; Nicolas et al., 1981). Diabases crop out in different styles in these ophiolites, including (1) lacking in the Alpine-Apennine ophiolites, (2) as dikes or sills intruding mantle peridotites and plutonic rocks in the Xigaze ophiolite, (3) comprising sheeted dike complexes in the Mirdita ophiolite, and (4) comprising sheeted sill complexes in the Xigaze and Coast Range ophiolites. Therefore, sheeted sill complexes occur only in the Xigaze and Cosat Range ophiolites, but have not been found in other ophiolites generated at slower-spreading ridges (Hopson, 2007). According to our model for the sheeted and non-sheeted sills in the Xigaze ophiolite, their generation needs a perfect sequence of events, including detachment faulting, and block exhumation, multi-stage rotations and foundering before dike propagation (Figure 15). The total rotation of the gabbro body is close to 90°. If block rotation and foundering is limited (e.g., during Stage 2-1 in Figure 15b), sill complexes are expected to rarely occur. This could explain why diabase dikes in drill cores, such as the Hole U1309D at the MAR and Hole 735B and U1473A at the SWIR, commonly cut other lithologies but show random orientations (e.g., Blackman et al., 2006; Dick et al., 2002, 2019b; Godard et al., 2009; MacLeod et al., 2002). On the other hand, bathymetric observations along ~2,500 km long region between 12.5°N and 35°N at the MAR revealed that asymmetrical accretions controlled by detachment faults cover nearly half of the ridge (Escartín et al., 2008). However, it is symmetrical accretion that dominates in the regions where detachment faults are rarely generated. In these regions, sheeted dike complexes are expected to be dominant, which are geometrically similar to those at fast-spreading ridges (Karson, 2018). Therefore, considering the complex crustal architectures at modern slow-spreading and ultraslow-spreading ridges, it is a perfect balance between block exhumation, rotation, and foundering that constructs the sheeted and non-sheeted pseudosills in the Xigaze ophiolite, which are almost unique in the world (Hopson, 2007; Nicolas et al., 1981).

## 7. Conclusions

Detailed field observations and structural measurements in this study have revealed variable diabase orientations in the Xigaze ophiolite, which could be subdivided into sheeted sills, non-sheeted sills and dikes. These diabases were probably emplaced at different stages, during or after the exhumation, rotation, foundering, and intense seawater alteration of the gabbros and mantle peridotites. This dynamic accretion of the Xigaze oceanic crust was intimately associated with the activities of oceanic detachment faults, which had also contributed to the deformation and high-temperature metamorphism of foliated gabbros and amphibolites in the serpentinized mantle peridotites. Block rotation and foundering, sometimes along with mass wasting, are suggested as two important controlling mechanisms reshaping the oceanic crustal architectures at asymmetrical segments of slow-spreading and ultraslow-spreading ridges. In contrast, sheeted dike

complexes are expected to be dominant at symmetrical segments of slower-spreading ridges, which hence have a similar geometry to those at fast-spreading ridges.

## Data Availability Statement

Original datasets for this paper are available in Mendeley Data (http://dx.doi.org/10.17632/x9fndtgn49.4).

**Acknowledgments**
The authors thank Ding-Shuai Xue, Yan-Hong Liu, Di Zhang, Li-Hui Jia, and Shi-Tou Wu for help in chemical analysis. We also acknowledge discussions with Yang Chu and Jia-Min Wang during the preparation of the manuscript. The authors are grateful to Editor-in-chief Claudio Faccenna and the associate editor for editorial handling, and Shu-Guang Song, Gianreto Manatschal, and anonymous reviewers for their constructive comments, which have significantly improved the quality of this paper. This study was financially supported by the National Natural Science Foundation of China (42025201 and 41802062), Key Research Program of Frontier Sciences from CAS (QYZDB-SSW-DQC032), Major Research project on Tethys Geodynamic System from NSFC (91755000), and Open Fund Project of State Key Laboratory of Lithospheric Evolution (201707).

## References

Agrinier, P., Javoy, M., & Girardeau, J. (1988). Hydrothermal activity in a peculiar oceanic ridge: Oxygen and hydrogen isotope evidence in the Xigaze ophiolite (Tibet, China). *Chemical Geology*, *71*, 313–335. https://doi.org/10.1016/0009-2541(88)90057-5

Alt, J. C., & Bach, W. (2006). Oxygen isotope composition of a section of lower oceanic crust, ODP Hole 735B. *Geochemistry, Geophysics, Geosystems*, *7*, Q12008. https://doi.org/10.1029/2006GC001385

Anderson, E. M. (1951). *The dynamics of faulting and dyke formation* (2nd ed.). London: Oliver and Boyd.

Bao, P. S., Su, L., Wang, J., & Zhai, Q. G. (2013). Study on the tectonic setting for the ophiolites in Xigaze, Tibet. *Acta Geologica Sinica (English Edition)*, *87*, 395–425.

Blackman, D. K., Canales, J. P., & Harding, A. (2009). Geophysical signatures of oceanic core complexes. *Geophysical Journal International*, *178*, 593–613. https://doi.org/10.1111/j.1365-246X.2009.04184.x

Blackman, D. K., Ildefonse, B., John, B. E., Ohara, Y., Miller, D. J., & MacLeod, C. J. (2006). Expedition 304/305 summary. In The Expedition 304/305 Scientists. Proc. IODP (Vol. 304/305). College Station TX: Integrated Ocean Drilling Program Management International, Inc. https://doi.org/10.2204/iodp.proc.304305.101.2006

Buck, R. W. (1988). Flexural rotation of normal faults. *Tectonics*, *7*, 959–973. https://doi.org/10.1029/TC007i005p00959

Cannat, M., Mangeney, A., Ondréas, H., Fouquet, Y., & Normand, A. (2013). High-resolution bathymetry reveals contrasting landslide activity shaping the walls of the Mid-Atlantic Ridge axial valley. *Geochemistry, Geophysics, Geosystems*, *14*, 996–1011. https://doi.org/10.1002/ggge.20056

Clayton, R. N., & Mayeda, T. K. (1963). The use of bromine pentafluoride in the extraction of oxygen from oxides and silicates for isotopic analysis. *Geochimica et Cosmochimica Acta*, *27*, 43–52. https://doi.org/10.1016/0016-7037(63)90071-1

Coogan, L. A., Wilson, R. N., Gillis, K. M., & MacLeod, C. J. (2001). Near-solidus evolution of oceanic gabbros: Insights from amphibole geochemistry. *Geochimica et Cosmochimica Acta*, *65*, 4339–4357. https://doi.org/10.1016/S0016-7037(01)00714-1

Dick, H. J. B., Kvassnes, A. J. S., Robinson, P. T., MacLeod, C. J., & Kinoshita, H. (2019a). The Atlantis Bank Gabbro Massif, Southwest Indian Ridge. *Progress in Earth and Planetary Science*, *6*, 64. https://doi.org/10.1186/s40645-019-0307-9

Dick, H. J. B., MacLeod, C. J., Blum, P., Abe N., Blackman D. K., Bowles J. A., et al. (2019b). Dynamic accretion beneath a slow spreading ridge segment: IODP Hole 1473A & the Atlantis Bank Oceanic Core Complex. *Journal of Geophysical Research Solid Earth*, *124*, 12631–12659. https://doi.org/10.1029/2018JB016858

Dick, H. J. B., Natland, J. H., & Ildefonse, B. (2006). Past and future impact of deep drilling in the oceanic crust and mantle. *Oceanography*, *19*, 72–80. https://doi.org/10.5670/oceanog.2006.06

Dick, H. J. B., Ozawa, K., Meyer, P. S., Niu, Y., Robinson, P. T., Constantin, M., et al. (2002). Primary silicate mineral chemistry of a 1.5-km section of very slow spreading lower ocean crust: ODP Hole 735B, Southwest Indian Ridge. *Proceedings of the Ocean Drilling Program, Scientific Results*, *176*, 1–61.

Drouin, M., Godard, M., Ildefonse, B., Bruguier, O., & Garrido, C. J. (2009). Geochemical and petrographic evidence for magmatic impregnation in the oceanic lithosphere at Atlantis Massif, Mid-Atlantic Ridge (IODP Hole U1309D, 30°N). *Chemical Geology*, *264*, 71–88. https://doi.org/10.1016/j.chemgeo.2009.02.013

Escartín, J., & Canales, J. P. (2011). Detachments in oceanic lithosphere: Deformation, magmatism, fluid flow, and ecosystems. *Eos*, *92*(4), 31.

Escartín, J., Mével C., Petersen S., Bonnemains D., Cannat M., Andreani M., et al. (2017). Tectonic structure, evolution, and the nature of oceanic core complexes and their detachment fault zones (13°20′N and 13°30′N, Mid Atlantic Ridge). *Geochemistry, Geophysics, Geosystems*, *18*, 1451–1482. https://doi.org/10.1002/2016GC006775

Escartín, J., Mével, C., MacLeod, C. J., & McCaig, A. M. (2003). Constraints on deformation conditions and the origin of oceanic detachments: The Mid-Atlantic Ridge core complex at 15°45′N. *Geochemistry, Geophysics, Geosystems*, *4*(8), 1067. https://doi.org/10.1029/2002GC000472

Escartín, J., Smith, D. K., Cann, J., Schouten, H., Langmuir, C. H., & Escrig, S. (2008). Central role of detachment faults in accretion of slow-spreading oceanic lithosphere. *Nature*, *455*, 790–795. https://doi.org/10.1038/nature07333

France, L., Ildefonse, B., & Koepke, J. (2009). Interactions between magma and hydrothermal system in Oman ophiolite and in IODP Hole 1256D: Fossilization of a dynamic melt lens at fast spreading ridges. *Geochemistry, Geophysics, Geosystems*, *10*, Q10O19. https://doi.org/10.1029/2009GC002652

Frassi, C., Musumeci, G., Zucali, M., Mazzarini, F., Rebay, G., & Langone, A. (2017). The Cotoncello Shear Zone (Elba Island, Italy): The deep root of a fossil oceanic detachment fault in the Ligurian ophiolites. *Lithos*, *278–281*, 445–463.

Gao, Y. J., Hoefs, J., Przybilla, R., & Snow, J. E. (2006). A complete oxygen isotope profile through the lower oceanic crust, ODP Hole 735B. *Chemical Geology*, *233*, 217–234. https://doi.org/10.1016/j.chemgeo.2006.03.005

Gass, I. G. (1968). Is the Troodos massif of Cyprus a fragment of Mesozoic ocean floor? *Nature*, *220*, 39–42. https://doi.org/10.1038/220039a0

Gerya, T. V., Perchuk, L. L., Triboulet, C., Audren, C., & Sez'ko, A. I. (1997). Petrology of the Tumanshet zonal metamorphic complex, Eastern Sayan. *Petrology*, *5/6*, 503–533.

Girardeau, J., Mercier, J. C. C., & Wang, X. B. (1985). Petrology of the mafic rocks of the Xigaze ophiolite, Tibet: Implications for the genesis of the oceanic lithosphere. *Contributions to Mineralogy and Petrology*, *90*, 309–321.

Girardeau, J., Mercier, J. C. C., & Zao, Y. G. (1985). Structure of the Xigaze ophiolite, Yarlung Zangbo suture zone, southern Tibet, China: genetic implications. *Tectonics*, *4*, 267–288. https://doi.org/10.1029/tc004i003p00267

Godard, M., Awaji, S., Hansen, H., Hellebrand, E., Brunelli, D., Johnson, K., et al. (2009). Geochemistry of a long in-situ section of intrusive slow-spread oceanic lithosphere: Results from IODP Site U1309 (Atlantis Massif, 30°N Mid-Atlantic-Ridge). *Earth and Planetary Science Letters*, *279*, 110–122. https://doi.org/10.1016/j.epsl.2008.12.034

Gong, B., Zheng, Y. F., & Chen, R. X. (2007). An online method combining a thermal conversion elemental analyzer with isotope ratio mass spectrometry for the determination of hydrogen isotope composition and water concentration in geological samples. *Rapid Communications in Mass Spectrometry*, *21*(8), 1386–1392.

Harmon, R. S., & Hoefs, J. (1995). Oxygen isotope heterogeneity of the mantle deduced from global 18O systematics of basalts from different geotectonic settings. *Contributions to Mineralogy and Petrology*, *120*(1), 95–114. https://doi.org/10.1007/BF00311010

Hébert, R., Bezard, R., Guilmette, C., Dostal, J., Wang, C. S., & Liu, Z. F. (2012). The Indus-Yarlung Zangbo ophiolites from Nanga Parbat to Namche Barwa syntaxes, southern Tibet: First synthesis of petrology, geochemistry, and geochronology with incidences on geodynamic reconstructions of Neo-Tethys. *Gondwana Research*, *22*, 377–397. https://doi.org/10.1016/j.gr.2011.10.013

Holland, T., & Blundy, J. (1994). Non-ideal interactions in calcic amphiboles and their bearing on amphibole-plagioclase thermometry. *Contributions to Mineralogy and Petrology*, *116*, 443–447. https://doi.org/10.1007/BF00310910

Hopson, C. A. (2007). Subvolcanic sheeted sills and nonsheeted dikes in ophiolites: Occurrence, origin, and tectonic significance for oceanic crust generation. *Geological Society of America Special Papers*, *419*, 225–254.

Hopson, C. A., Mattinson J. M., Pessagno E., & Luyendyk B. P. (2008). California Coast Range ophiolite: Composite Middle and Late Jurassic oceanic lithosphere. *GSA Special Papers*, *438*, 1–101.

Ildefonse, B., Blackman, D. K., John, B. E., Ohara, Y., Miller, D. J., MacLeod, C. J., et al. (2007). Oceanic core complexes and crustal accretion at slow-spreading ridges. *Geology*, *35*, 623–626. https://doi.org/10.1130/G23531A.1

Karson, J. A. (2018). From ophiolites to oceanic crust: Sheeted dike complexes and seafloor spreading. In R. K. Srivastava, R. Ernst, & P. Peng (Eds.), *Dyke swarms of the world: A modern perspective,* Springer Geology (pp. 459–492). Singapore: Springer. https://doi.org/10.1007/978-981-13-1666-1_13

Kelemen, P. B., Kikawa, E., Miller, D. J., & Shipboard Scientific Party (2007). Leg 209 summary: Processes in a 20-km-thick conductive boundary layer beneath the Mid-Atlantic Ridge, 14°–16°N. In P. B. Kelemen, E. Kikawa, & D. J. Miller (Eds.), Proc. ODP, Sci. Results (Vol. 209, pp. 1–33). College Station, TX: Ocean Drilling Program. https://doi.org/10.2973/odp.proc.sr.209.001.2007

Kinzler, R. J., & Grove, T. L. (1993). Corrections and further discussion of the primary magmas of mid-ocean ridge basalts, 1 and 2. *Journal of Geophysical Research*, *98*, 22339–22347. https://doi.org/10.1029/93JB02164

Lagabrielle, Y., & Cannat, M. (1990). Alpine Jurassic ophiolites resemble the modern central Atlantic basement. *Geology*, *18*, 319–322.

Lagabrielle, Y., Vitale Brovarone, A., & Ildefonse, B. (2015). Fossil oceanic core complexes recognized in the blueschist metaophiolites of Western Alps and Corsica. *Earth-Science Reviews*, *141*, 1–26.

Lavier, L. L., Buck, W. R., & Poliakov, A. N. B. (1999). Self-consistent rolling-hinge model for the evolution of large-offset low-angle normal faults. *Geology*, *27*, 1127–1130. http://doi.org/10.1130/0091-7613(1999)027<1127:SCRHMF>2.3.CO;2

Li, Y., Li, R. B., Dong, T. C., Yang, S. B., & Pei, L. (2016). Structure of the Baimarang massif in the Xigaze ophiolite, Yarlung Zangbo Suture Zone, southern Tibet, China(in Chinese with English abstract). *Chinese Science Bulletin*, *61*, 2823–2833. https://doi.org/10.1360/N972016-00203

Liu, T., Wu, F. Y., Liu, C. Z., Eyuboglu, Y., Zhu, D. C., Zhang, C., et al. (2020). Testing oceanic crust–mantle decoupling by Sr–Nd–Hf–Os isotopes of Neo-Tethyan ophiolites. *Lithos*, *376–377*, 105757. https://doi.org/10.1016/j.lithos.2020.105757

Liu, T., Wu, F. Y., Liu, C. Z., Tribuzio, R., Ji, W. B., & Zhang, C., (2018). Variably evolved gabbroic intrusions within the Xigaze ophiolite (Tibet): new insights into the origin of ophiolite diversity. *Contributions to Mineralogy and Petrology*, *173*, 91. https://doi.org/10.1007/s00410-018-1518-6

Liu, T., Wu, F. Y., Liu, C. Z., Zhang, C., Ji, W. B., & Xu, Y. (2019). Reconsideration of Neo-Tethys evolution constrained from the nature of the Dazhuqu ophiolitic mantle, southern Tibet. *Contributions to Mineralogy and Petrology*, *174*, 23. https://doi.org/10.1007/s00410-019-1557-7

Liu, T., Wu, F. Y., Zhang, L. L., Zhai, Q. G., Liu, C. Z., Ji, W. B., et al. (2016). Zircon U-Pb geochronological constraints on rapid exhumation of the mantle peridotite of the Xigaze ophiolite, southern Tibet. *Chemical Geology*, *443*, 67–86. https://doi.org/10.1016/j.chemgeo.2016.09.015

MacLeod, C. J., Carlut, J., Escartín, J., Horen, H., & Morris, A. (2011). Quantitative constraint on footwall rotations at the 15°45′N oceanic core complex, Mid-Atlantic Ridge: Implications for oceanic detachment fault processes. *Geochemistry, Geophysics, Geosystems*, *12*, Q0AG03. https://doi.org/10.1029/2011GC003503

MacLeod, C. J., Dick, H. J. B., Blum, P., Abe, N., Blackman, D. K., Bowles, J. A., et al. (2017). Site U1473. In C. J. MacLeod, H. J. B. Dick, P. Blum, & the Expedition 360 Scientists (Eds.), In Southwest Indian Ridge Lower Crust and Moho. Proceedings of the International Ocean Discovery Program (Vol. 360). College Station, TX: International Ocean Discovery Program. https://doi.org/10.14379/iodp.proc.360.103.2017

MacLeod, C. J., Escartín, J., Banerji, D., Banks, G. J., Gleeson, M., Irving, D. H. B., et al. (2002). Direct geological evidence for oceanic detachment faulting: The Mid-Atlantic Ridge, 15°45′N. *Geology*, *30*, 879–882. https://doi.org/10.1130/0091-7613(2002)0302.0.CO;2

MacLeod, C. J., Searle, R. C., Murton, B. J., Casey, J. F., Mallows, C., Unsworth, S. C., et al. (2009). Life cycle of oceanic core complexes. *Earth and Planetary Science Letters*, *287*, 333–344. https://doi.org/10.1016/j.epsl.2009.08.016

Maffione, M., Morris, A., & Anderson, M. W. (2013). Recognizing detachment-mode seafloor spreading in the deep geological past. *Scientific Reports*, *3*, 2336. https://doi.org/10.1038/srep02336

Maffione, M., van Hinsbergen, D. J. J., Koornneef, L. M. T., Guilmette, C., Hodges, K., Borneman, N., et al. (2015). Forearc hyperextension dismembered the south Tibetan ophiolites. *Geology*, *43*, 475–478. https://doi.org/10.1130/g36472.1

Manatschal, G., Sauter, D., Karpoff, A. M., Masini, E., Mohn, G., & Lagabrielle, Y. (2011). The Chenaillet Ophiolite in the French/Italian Alps: An ancient analogue for an Oceanic Core Complex?. *Lithos*, *124*, 169–184.

Manning, C. E., Weston, P. E., & Mahon, K. I. (1996). Rapid high-temperature metamorphism of East Pacific Rise gabbros from Hess Deep. *Earth and Planetary Science Letters*, *144*, 123–132. https://doi.org/10.1016/0012-821x(96)00153-7

Moores, E. M., & Vine, F. J. (1971). The Troodos massif, Cyprus, and other ophiolites as oceanic crust: evaluation and implications. *Philosophical Transactions Royal Society, London, A*, *268*, 443–466. https://doi.org/10.1098/rsta.1971.0006

Morris, A., Gee, J. S., Pressling, N., John, B.E., MacLeod, C. J., Grimes, C. B., & Searle, R. C. (2009). Footwall rotation in an oceanic core complex quantified using reoriented Integrated Ocean Drilling Program core samples. *Earth and Planetary Science Letters*, *287*, 217–228. https://doi.org/10.1016/j.epsl.2009.08.007

Muehlenbachs, K., & Clayton, R. N. (1972). Oxygen isotope studies of fresh and weathered submarine basalts. *Canadian Journal of Earth Sciences*, *9*, 172–184. https://doi.org/10.1139/e72-014

Nicolas, A., Boudier, F., & Ceuleneer, G. (1988). Mantle flow patterns and magma chambers at ocean ridges: Evidence from the Oman ophiolite. *Marine Geophysical Research*, *9*, 293–310. https://doi.org/10.1007/bf00315002

Nicolas, A., Boudier, F., & Meshi, A. (1999). Slow spreading accretion and mantle denudation in the Mirdita ophiolite (Albania). *Journal of Geophysical Research*, *104*, 15155–15167.

Nicolas, A., Girardeau, J., Marcoux, J., Dupre, B., Wang, X. B., Cao, Y. G., et al. (1981). The Xigaze Ophiolite (Tibet): a peculiar oceanic lithosphere. *Nature*, *294*, 414–417. https://doi.org/10.1038/294414a0

Nicolas, A., Meshi, A., Boudier, F., Jousselin, D., & Muceku, B. (2017). Mylonites in ophiolite of Mirdita (Albania): Oceanic detachment shear zone. *Geosphere*, *13*, 136–154. https://doi.org/10.1130/GES01383.1

Parnell-Turner, R., Sohn, R. A., Peirce, C., Reston, T. J., MacLeod, C. J., Searle, R. C., & Simao, N. M. (2017). Oceanic detachment faults generate compression in extension. *Geology*, *45*, 923–926. https://doi.org/10.1130/G39232.1

Sanfilippo, A., Dick, H. J. B., Marschall, H. R., Lissenberg, C. J., & Urann, B. (2019). Emplacement and high-temperature evolution of gabbros of the 16.5°N oceanic core complexes (Mid-Atlantic Ridge): Insights into the compositional variability of the lower oceanic crust. *Geochemistry, Geophysics, Geosystems*, *20*, 46–66. https://doi.org/10.1029/2018GC007512

Sanfilippo, A., & Tribuzio, R. (2011). Melt transport and deformation history in a nonvolcanic ophiolitic section, northern Apennines, Italy: Implications for crustal accretion at slow spreading settings. *Geochemistry, Geophysics, Geosystems*, *12*, Q0AG04. https://doi.org/10.1029/2010GC00342

Sauter, D., Cannat, M., Rouméjon, S., Andreani, M., Birot, D., Bronner, A., et al. (2013). Continuous exhumation of mantle-derived rocks at the Southwest Indian Ridge for 11 million years. *Nature Geoscience*, *6*, 314–320. https://doi.org/10.1038/NGEO1771

Sinton, J. M., & Detrick, R. S. (1992). Mid-ocean ridge magma chambers. *Journal of Geophysical Research*, *97*, 197–216.

Smith, D. K., Schouten H., Dick H. J. B., Cann J. R., Salters V., Marschall H. R., et al. (2014). Development and evolution of detachment faulting along 50 km of the Mid-Atlantic Ridge near 16.5°N. *Geochemistry, Geophysics, Geosystems*, *15*, 4692–4711. https://doi.org/10.1002/2014GC005563

Snow, J. E., & Edmonds, H. N. (2007). Ultraslow-spreading ridges rapid paradigm changes. *Oceanography*, *20*, 90–101. https://doi.org/10.5670/oceanog.2007.83

Stakes, D. S., & Taylor, H. P. (1992). The northern Samail ophilite: An oxygen isotope, microprobe, and field study. *Journal of Geophysical Research*, *97*, 7043–7080.

Suhr, G., Hellebrand, E., Johnson, K., & Brunelli, D. (2008). Stacked gabbro units and intervening mantle: A detailed look at a section of IODP Leg 305, Hole U1309D. *Geochemistry, Geophysics, Geosystems*, *9*, Q10007. https://doi.org/10.1029/2008GC002012

Sun, S. S., & McDonough, W. (1989). Chemical and isotopic systematics of oceanic basalts: Implications for mantle composition and processes. *Geological Society, London, Special Publications*, *42*, 313–345. https://doi.org/10.1144/GSL.SP.1989.042.01.19

Taylor, H. P., & Sheppard, S. M. F. (1986). Igneous Rocks: I. In J. W. Valley, H. P. Taylor, & J. R. O'Neil (Eds.), Stable isotopes in high-temperature geological processes, Rev. Mineral. (Vol. 16, pp. 277–271). Washington, DC: Mineral. Society of America.

Tribuzio, R., Renna, M. R., Dallai, L., & Zanetti, A. (2014). The magmatic-hydrothermal transition in the lower oceanic crust: Clues from the Ligurian ophiolites, Italy. *Geochimica et Cosmochimica Acta*, *130*, 188–211. https://doi.org/10.1016/j.gca.2014.01.010

Tucholke, B. E., Behn, M. D., Buck, W. R., & Lin, J. (2008). Role of magma supply in oceanic detachment faulting and formation of megamullions. *Geology*, *36*, 455–458. https://doi.org/10.1130/G24639A.1

Wu, F. Y., Liu, C. Z., Zhang, L. L., Zhang, C., Wang, J. G., Ji, W. Q., & Liu, X. C. (2014). Yarlung Zangbo ophiolite: A critical updated view(in Chinese with English abstract). *Acta Petrologica Sinica*, *30*, 293–325. https://doi.org/10.0569/2014/030(02)-0293-25

Yin, A., & Harrison, T. M. (2000). Geologic evolution of the Himalayan-Tibetan orogen. *Annual Review of Earth and Planetary Sciences*, *28*, 211–280. https://doi.org/10.1146/annurev.earth.28.1.211

Zhang, C., Liu, C. Z., Wu, F. Y., Ji, W. B., Liu, T., & Xu, Y. (2017). Ultra-refractory mantle domains in the Luqu ophiolite (Tibet): Petrology and tectonic setting. *Lithos*, *286–287*, 252–263. https://doi.org/10.1016/j.lithos.2017.05.021

Zhang, L. L., Liu, C. Z., Wu, F. Y., Zhang, C., Ji, W. Q., & Wang, J. G. (2016). Sr-Nd-Hf isotopes of the intrusive rocks in the Cretaceous Xigaze ophiolite, southern Tibet: Constraints on its formation setting. *Lithos*, *258–259*, 133–148. https://doi.org/10.1016/j.lithos.2016.04.026

Zhang, W. Q., Liu, C. Z., & Dick, H. J. B. (2020). Evidence for multi-stage melt transport in the lower ocean crust: Atlantis Bank Gabbroic Massif (IODP Hole U1473A, SW Indian Ridge). *Journal of Petrology*, *61*, egaa082. https://doi.org/10.1093/petrology/egaa082/5890488